

Cislunar Periodic Orbit Families and Expected Observational Features

C. Channing Chow¹, Charles J. Wetterer¹, Keric Hill¹,
Claire Gilbert¹, David Buehler², and James Frith²

¹Pacific Defense Solutions – a Centauri Company

²Air Force Research Laboratory

ABSTRACT

Orbits of objects in cislunar space are non-Keplerian due to the influence of the Moon’s gravity and cannot be generically parameterized by a simple set of characteristics. Objects are also fainter and move relatively more slowly when viewed from the Earth; both detection and tracking are expected to be significantly more difficult. In this paper we review a subset of possible orbits and their expected astrometric and photometric signatures from the perspective of hypothetical ground-based sensors on the Earth and Moon. Although a multitude of orbits are possible, we focus on special types of orbits that are closed in the synodic frame (i.e., periodic) and emanate from the libration points (stationary equilibria of the circular restricted three-body problem). We investigate 31 separate families of elemental periodic orbits (Doedel et al., 2007), each of which are smooth manifolds. For each family, we generate a span of representative synodic positions and velocities and simulate the expected observational features (e.g., right ascension, declination, visual magnitude) based on faceted satellite models. In this study, we hope to build a better intuition on how remote sensing will work for spacecraft in cislunar space, to support next-generation sensor architectures including space-based experiments such as AFRL’s Cislunar Highway Patrol System (CHPS) concept.

1. INTRODUCTION

Cislunar space is a term that is becoming very prominent in the space community lately. Although it is a term generally meaning “lying between the Earth and Moon”, more formal boundaries are useful for practical considerations, such as determining operational limits for cislunar traffic management or for selecting sufficient dynamical systems approximations for initial orbit determination (IOD).

The proposed definition of cislunar space compartmentalizes the spatial volume into *five* distinct “zones” (see .) derived from volumes roughly corresponding to energy boundaries. Equivalently, the zones are regions where a particular gravitational body dominates or where multiple bodies must be considered. These zones are analogous to more familiar concepts such as low-Earth orbit (LEO) and geostationary equatorial orbit (GEO) which are both, in fact, zero-velocity surfaces for the restricted two-body problem.

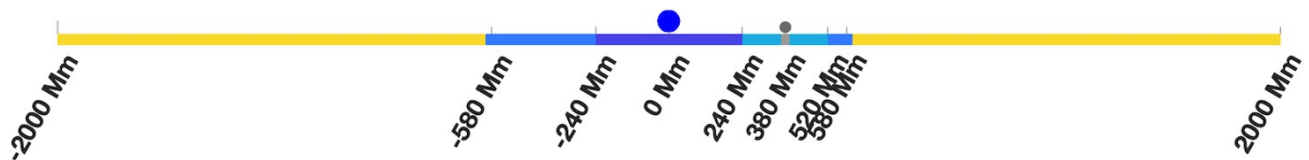


Figure 1. Cislunar space zones (to scale) projected in one dimension. Earth Zone is dark blue, Moon Zone is grey, Earth-Moon Zone is teal, Sun-Earth-Moon Zone is light blue, and Sun-Earth Zone is gold.

Table 1. Zone definitions for Cislunar Space. The additional LEO and GEO regions are part of the Earth zone.

Zone	Center	Radius	Dominant Dynamics
Earth	Earth	240,000 km	*2-body Earth
-GEO	Earth	42,164 km	*2-body Earth
-LEO	Earth	2,000 km	*2-body Earth
Moon	Moon	14,000 km	*2-body Moon
Earth-Moon	Moon	140,000 km	*3-body Earth-Moon
Sun-Earth-Moon	Earth	580,000 km	*4-body Sun-Earth-Moon
Sun-Earth	Earth	2,000,000 km	*3-body Sun-Earth

*restricted

This separation into zones is somewhat arbitrary, in terms of the specific value of the boundaries (see *Table 1*), but logical, in terms of the structure, since it (1) follows the zero-velocity surface contours of the circular restricted three-body problem (CR3BP) and (2) is supported with numerical analysis of the averaged time-varying gravitational perturbations in the area. *Figure 2* shows the zones overlaid on top of a zero-velocity surface map for the CR3BP for the Earth-Moon system (an upper limit Jacobi value of 3.6 is used to highlight energy levels that are consistent with the boundary limits). While the zero-velocity surfaces do not admit exactly spherical regions about the Earth, Moon, or any other region, we approximate these zones as “spheres” to simplify their description.

The main reason for identifying the zones is to illustrate how the dominant dynamics differ across regions in cislunar space. Traditional space domain awareness (SDA) takes place almost entirely in the lower ~20% of the Earth zone. When venturing beyond GEO¹, the Moon and the Sun can no longer be considered negligible distant perturbations.

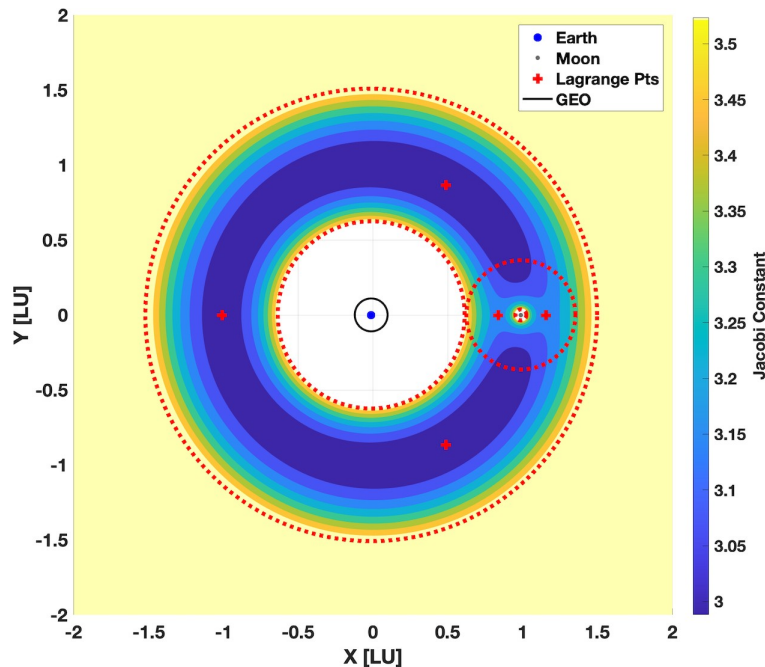


Figure 2. Zero-velocity surface map for cislunar space. Colors represent different values of Jacobi constant, equivalent to energy bounds. Red dashed lines represent various zone limits. Earth and Moon are not plotted to scale. Regions above $C_j = 3.6$ and $r > 1.5$, are level set to preserve finer contour detail.

¹ The phrase “beyond GEO”, to some, has become known as “XGEO”. For the purposes of this paper, we consider XGEO to be synonymous to “cislunar”.

Counter to intuitions built around near-Earth (i.e., roughly GEO and below) SDA, there are some notable challenges associated with considering cislunar orbits. For example, the ubiquitous two-line element (TLE) will no longer suffice. Since cislunar orbits are often not representable by conic sections (i.e., non-Keplerian), they cannot be generically parameterized by a simple set of characteristics or elements. Furthermore, observing objects in cislunar space is harder – objects are both fainter (longer distances will stress remote sensing capabilities) and slower (longer time scales mean more observations are necessary to see significant fractions of orbits). Tracking is harder – cislunar objects do not travel in approximate planes. Detection is harder – a cislunar object’s relative motion is closer to that of the stars than to near-Earth satellites. In terms of prediction and correction (the tenets of estimation), since cislunar dynamics approach the chaos boundary, where small perturbations can lead to wildly disproportionate outcomes, traditional data processing techniques (e.g., IOD) become far more difficult.

To better understand how to overcome these challenges, we present a survey study on a sample space of cislunar orbits and corresponding observable metrics as measured from hypothetical ground-based sensors on the Earth and the Moon. We hope to inform the community’s intuition on how to extend legacy capabilities into next-generation capabilities in preparation for handling the nuances of cislunar space.

2. PERIODIC ORBITS

In this paper we employ the CR3BP: a highly idealized dynamical system which considers only the gravitational perturbations of the primaries (e.g., Earth and Moon). The primaries are assumed to revolve in concentric circles around their mutual barycenter such that the distance between the primaries remains fixed. This system admits exactly 5 equilibria (libration or Lagrange points, $\mathcal{L}1 - \mathcal{L}5$) as shown in Figure 2. The Jacobi constant (Eq. 1) is the only known conserved quantity for the CR3BP. It is a useful scalar with which to parametrize orbits much like an energy value.

$$C_1 = n^2(x^2 + y^2) + 2\sqrt{5}\frac{\mu_{\#}}{r_{\#}} + \frac{\mu^*}{r^*} - (\dot{x}^2 + \dot{y}^2 + \dot{z}^2) \quad (1)$$

where n is the mean motion, and $\mu_{\#}/r_{\#}$ and μ^*/r^* are the mass per distance ratios of the larger and smaller primaries, respectively. The remaining variables (x, y) and $(\dot{x}, \dot{y}, \dot{z})$ are the synodic position (note, there is no explicit dependence on z) and velocity coordinates, respectively. The characteristic non-dimensionalized quantities for the Earth-Moon system are: Length Unit (LU) = 384,400 km, Time Unit (TU) = 4.348 days, and Mass Ratio (μ) = 0.01215.

In general, periodic orbits are special types of solutions of a dynamical system of the form,

$$\frac{dX}{dt} = f(X, t) \quad (2)$$

that satisfy the definition,

$$X(t) = X(t + T), \quad \forall t \in \mathbb{R}^{\#} \quad (3)$$

Thus, after one period, T , these orbits are “closed” or “repeat” in time (generally only in the synodic frame). Periodic orbits are not necessarily isolated solutions; in the CR3BP we find periodic orbit families of solutions, generated by smoothly varying a continuation parameter (Keller, 1977) such as the period.

DISTRIBUTION STATEMENT A: Approved for public release. Distribution unlimited.

The particular periodic orbit families or manifolds in this discussion emanate from the CR3BP libration points, then bifurcate into various other families at branch points. The set of elemental periodic orbit families for the Earth-Moon system is listed in Table 2 and shown schematically in Figure 3. In our case, we consider 31 distinct families. In terms of notation, “HN2” and “HS2” designates the northern and southern halves, respectively, of the halo family emanating from libration point $\mathcal{L}2$.

Each family forms a smooth manifold. Some of these manifolds have distinguishable structures: planar (e.g., Lyapunov families), continuously North-South symmetric (e.g., Vertical families), North-South reflective (e.g., HN2 and HS2), or continuously East-West symmetric (e.g., W4W5).

Table 2. Elemental periodic orbit families for $\mu = 0.01215$.

Family grouping	Family designators	Branch points
Long and short period planar Lyapunov	L1, L2, L3, L4, L5, S3	L11 (L1/H1), L12 (L1/A1), L21 (L2/HN2/HS2), L22 (L2/A2), L24 (L2/RN2/RS2), L31 (L3/HN3/HS3), L32 (L3/A3), L33 (L3/S3), S41 (L4/S3), S51 (L5/S3), $\mathcal{L}1$ (L1/V1), $\mathcal{L}2$ (L2/V2), $\mathcal{L}3$ (L3/V3), $\mathcal{L}4$ (L4/V4V5/S3), $\mathcal{L}5$ (L5/V4V5/S3)
Vertical	V1, V2, V3, V4V5	V11 (V1/A1), V12 (V1/BN1/BS1), V21 (V2/A2), V22 (V2/BN2/BS2), V31 (V3/A3), V32 (V3/B3), V41 (V4V5/W4W5), V45 (V3/V4V5), V51 (V4V5/W4W5), C11 (C1/V1), C22 (C2/V2), C23 (C2/V3), $\mathcal{L}1$ (L1/V1), $\mathcal{L}2$ (L2/V2), $\mathcal{L}3$ (L3/V3), $\mathcal{L}4$ (L4/V4V5/S3), $\mathcal{L}5$ (L5/V4V5/S3)
Halo	H1, HN2, HS2, HN3, HS3	H11 (H1/W4W5), L11 (L1/H1), L21 (L2/HN2/HS2), L31 (L3/HN3/HS3), C21 (C2/H1)
Axial	A1, A2, A3	L12 (L1/A1), L22 (L2/A2), L32 (L3/A3), V11 (V1/A1), V21 (V2/A2), V31 (V3/A3)
Backflip	BN1, BS1, BN2, BS2, B3	V12 (V1/BN1/BS1), V22 (V2/BN2/BS2), V32 (V3/B3), D11 (D1/B3)
Circular	C1, C2	C11 (C1/V1), C21 (C2/H1), C22 (C2/V2), C23 (C2/V3)
Other	D1, EN1, ES1, RN2, RS2, W4W5	D11 (D1/B3), D12 (D1/EN1/ES1), L24 (L2/RN2/RS2), V41 (V4V5/W4W5), V51 (V4V5/W4W5), H11 (H1/W4W5)

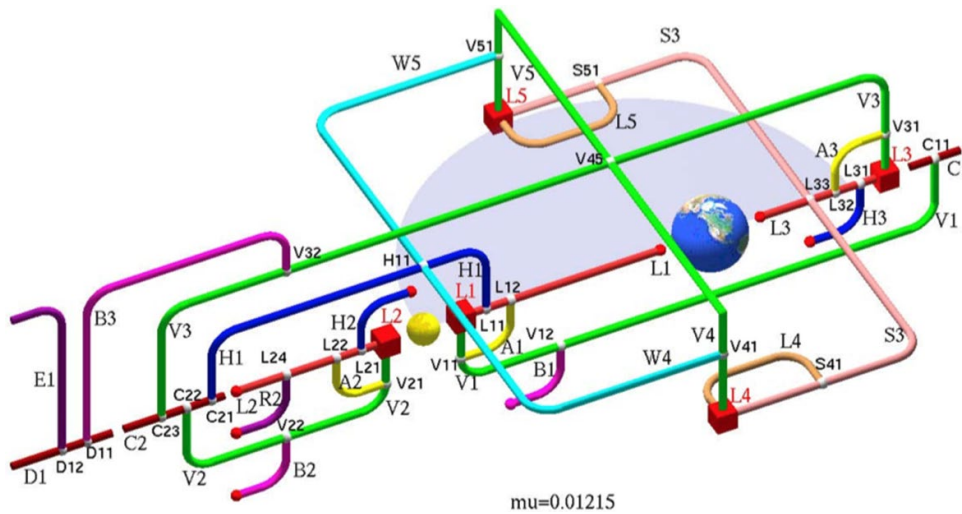


Figure 3. Bifurcation diagram of elemental periodic orbit families for the Earth-Moon system (Doedel et al., 2007).

DISTRIBUTION STATEMENT A: Approved for public release. Distribution unlimited.

Figure 4 depicts the HS2 family (contains the near-rectilinear halo orbits – NRHO – about $\mathcal{L}2$), which is primarily elongated south of the Moon’s orbital plane. At one extreme, the HS2 family bifurcates from the L21 branch point (connected to the L2 family), and at the other extreme, the manifold terminates in a collision orbit with the Moon. A representative “target orbit” is shown in red in Figure 4 along with its orthogonal projections to better highlight one member amongst the family. Plots include representations in both the synodic and sidereal frames – in inertial space, it is obvious that the target halo orbit is not even close to an ellipse. See the Appendix for similar plots depicting all 31 elemental periodic orbit families described in Table 2.

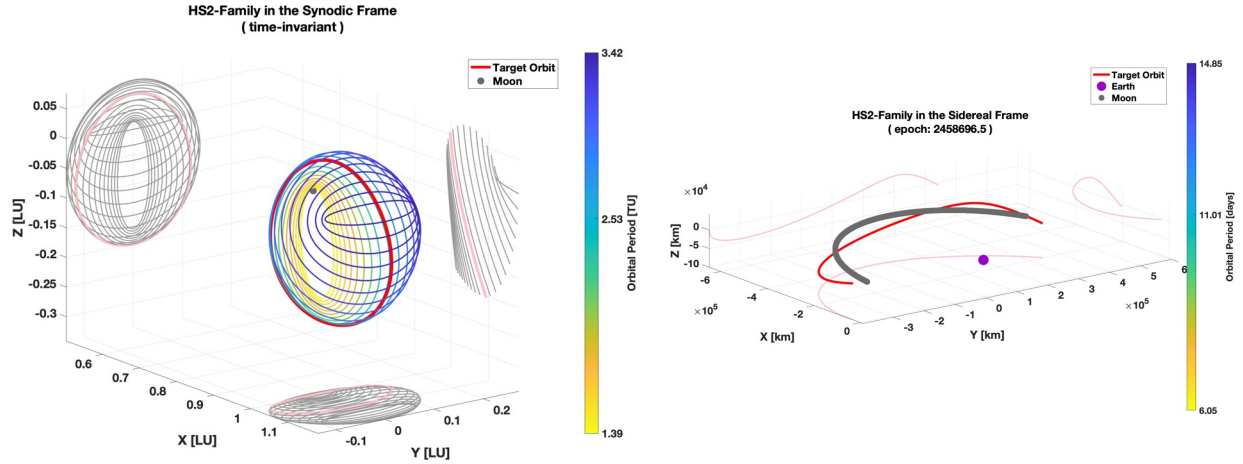


Figure 4. (left) HS2 family in the synodic frame and (right) sample HS2 target orbit in the sidereal frame for epoch 2019.08.01.

An orbital data set is constructed by sampling the span of each of the 31 continuous elemental periodic orbit families into 512 representative orbits. Each orbit contains 1024 ephemeris points regularly spaced in time over the span of the orbit’s period (the time step is orbit dependent)². This data set thus amounts to 16,252,928 individual state vectors and serves as the foundation for all of the following synthetic observation modeling and simulation.

3. EXTRACTING OBSERVATIONAL FEATURES

With the orbital data set providing the ephemerides for the set of elemental periodic orbit families in the synodic frame, we next model hypothetical sensors with which to observe targets traveling in these paths. For near-Earth sensors, it is necessary to first transform the orbital data from the synodic frame to the sidereal frame. This transformation involves aligning the actual state of the Moon at the epoch of interest (since the synodic frame is time-invariant) and compensating for the mean rotational rate of the rotating frame with respect to the inertial frame as well as the barycenter offset.

Since the order of linear operations matters here, the first step is to account for the shift in barycenter (Eq. 4); the (') indicates an intermediate state. Then, we must move to correct for the epoch and unmatched the rotational rate of the rotating frame (Eq. 5); the (") indicates another intermediate state.

$$\mathbf{X}' = \mathbf{X}_{\text{synodic}} \mathbf{C}^* - \mathbf{X}_{\text{Earth}} \quad (4)$$

$$\mathbf{X}'' = \begin{bmatrix} \Gamma & \mathbf{0}_{0 \times 0} & \mathbf{0}_{2 \times 1} \\ \mathbf{I} & \Gamma & \Gamma \end{bmatrix} \mathbf{L} \mathbf{X}' \quad (5)$$

² The choice of discretization in powers of two is made to benefit downstream machine learning algorithms (Martin et al., 2020).
DISTRIBUTION STATEMENT A: Approved for public release. Distribution unlimited.

The variable ν represents the spectral band of a sensor. M_{\odot} is the Sun's visual magnitude. F_{A4} is the target's flux and F_{\odot} is the solar flux.

The fidelity of the simulation of the apparent visual magnitude thus depends on the accuracy with which one models the target's flux. For this study, we use our forward lightcurve modeling software – Forge – to generate all of the photometric observables. Forge models satellites by constructing arbitrarily complex 3D shapes from combinations of discrete facets. The contribution from each facet is calculated separately based on the facet's bidirectional reflectance distribution function (BRDF) and the orientation of that facet with respect to the illumination source (e.g., the Sun) and the observer. We do not consider any intrinsic luminosity of the target nor self-shadowing.

4. MODELING AND SIMULATION RESULTS

In this paper we show results from two use cases:

1. Astrometric and photometric signatures of a sample satellite in select HS2 orbits as seen from three different ground-based Earth sensors.
2. Astrometric and photometric signatures of a sample satellite in select H1, HN2, and HS2 orbits as seen from two different ground-based Moon sensors.

In both cases, the sample satellite is modeled as a 2-meter diameter diffuse sphere approximated by 100 surface facets each with an average reflectance of 0.5. Different wavebands are selected by specifying the corresponding apparent solar magnitude. For example, we select the Johnson-R filter band with $M_{\odot} = -26.96597$. The ECI Sun, Moon, and sensor positions are calculated as functions of time, specifically, Julian date (Vallado, 2013). Visibility is determined by satisfying all of the following criteria:

- Target is above the sensor's local horizon
- Target is within Earth's or Moon's umbral or penumbral shadow
- For Earth-based platforms:
 - Sun is below sensor's local horizon (due to atmospheric scattering)
 - Target is outside of Moon exclusion zone
- For Moon-based platforms:
 - Target is outside of Earth and Sun exclusion zones

4.1 Observables of Targets in HS2 from Earth-based Sensors

Entering with the understanding that a single ground-based Earth sensor will not be able to achieve continuous coverage of a cislunar target, we choose to model several disparate sensors to simulate a hypothetical network that would be able to, at minimum, maintain near continuous coverage over a particular timeframe.

Sensor setup: Basing is on Earth. Three hypothetical optical sensors are chosen at the following geographic sites:

- Maui (20.7° N, 156.4° W)
- Azores (37.8° N, 25.5° W)
- Cocos Islands (12.2° S, 96.9° E)

The timeframe for the simulation is 122 days (01 Aug 2019 – 30 Nov 2019); each sensor's observation interval is set to 1 hour. Pristine (i.e., no added uncertainty) lightcurves are computed to include only observations that meet the visibility criteria. The Moon exclusion zone is arbitrarily set at 1° from its center.

Target setup: HS2 is selected as the host elemental periodic orbit family. Three different orbits are sampled from the 512 available in our orbital data set: orbit 50, 250, and 450. Three different starting points are allowed out of 1024 times that span the beginning and end of one orbital period: time step 1, 409, and 817. The various HS2 orbital periods range from approximately 6.05 to 14.85 days.

For context, the right ascension (RA), declination (DEC), and lightcurve (mag) plots for the same sample target in GEO (specifically, a geostationary object at the longitude of Maui) are presented. Figure 5 shows the right ascension changing at the sidereal rate and the declination as constant, which is consistent when considering that the azimuth

DISTRIBUTION STATEMENT A: Approved for public release. Distribution unlimited.

and elevation is fixed for this sensor-target geometry. A single night's lightcurve is also shown, with a small gap at peak brightness corresponding to a near-zero solar phase angle before entering (and then exiting) Earth's shadow.

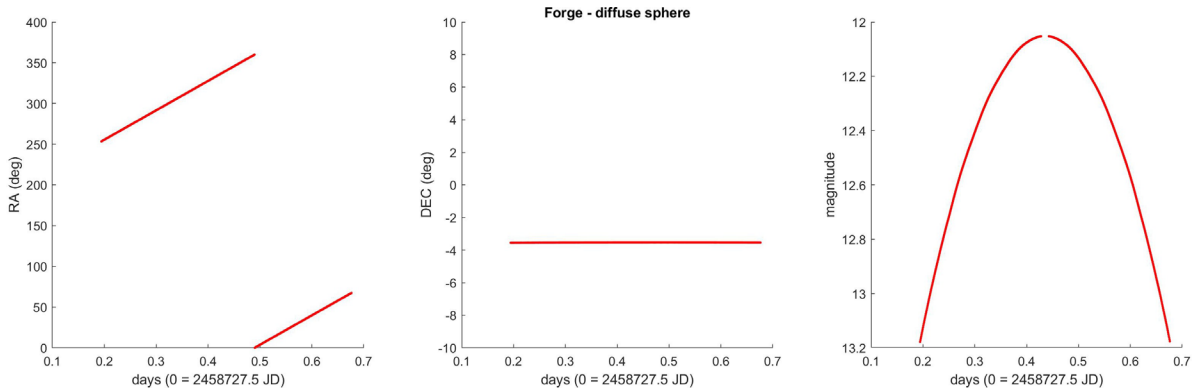


Figure 5. RA/DEC and magnitude observations of a diffuse sphere in GEO as observed from Maui for one night.

Figure 6 shows the simulated observations for the diffuse sphere case. Each row shows a different HS2 orbit, and each column shows a different observable. The timeframe spans the entire scenario. Each target is located at the “start” of each of their respective orbits (as defined in the construction of the orbital data set). Each sensor’s response is color-coded (red: Maui, blue: Azores, cyan: Cocos Islands). Since a fair amount of data is plotted, certain details are hard to distinguish; therefore, Figure 7 shows a zoomed-in portion of the data to highlight a 10 day window.

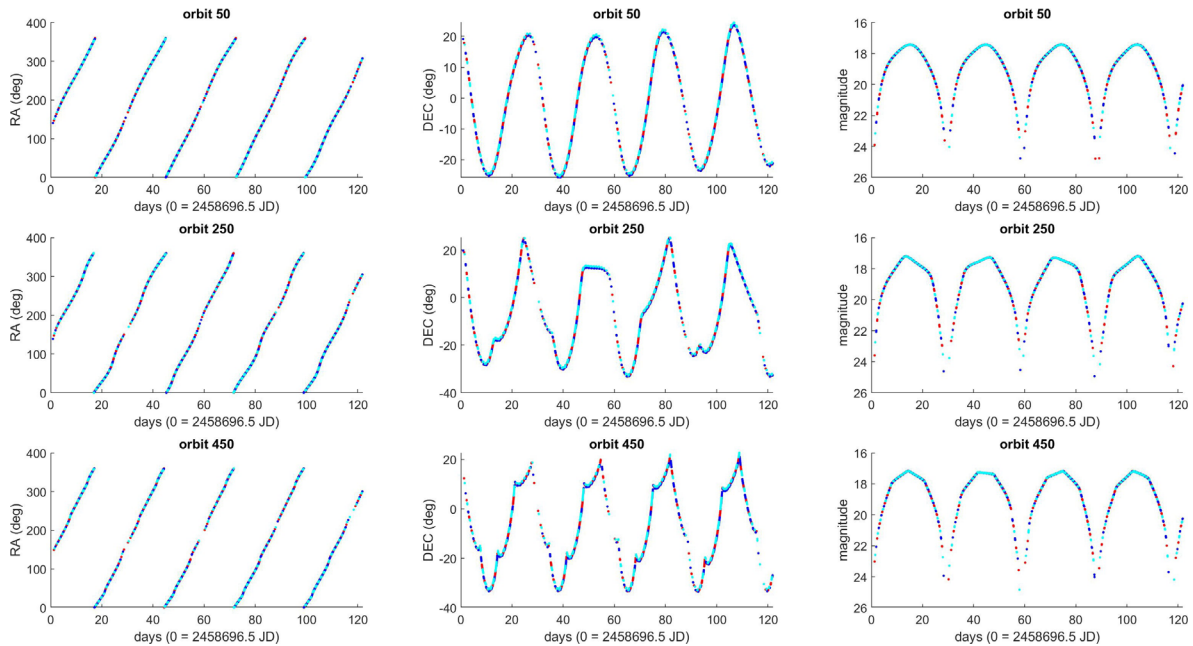


Figure 6. RA/DEC and magnitude observations over the entire 122 days for diffuse spheres in HS2 orbits 50, 250, and 450 (red: Maui, blue: Azores, cyan: Cocos Islands).

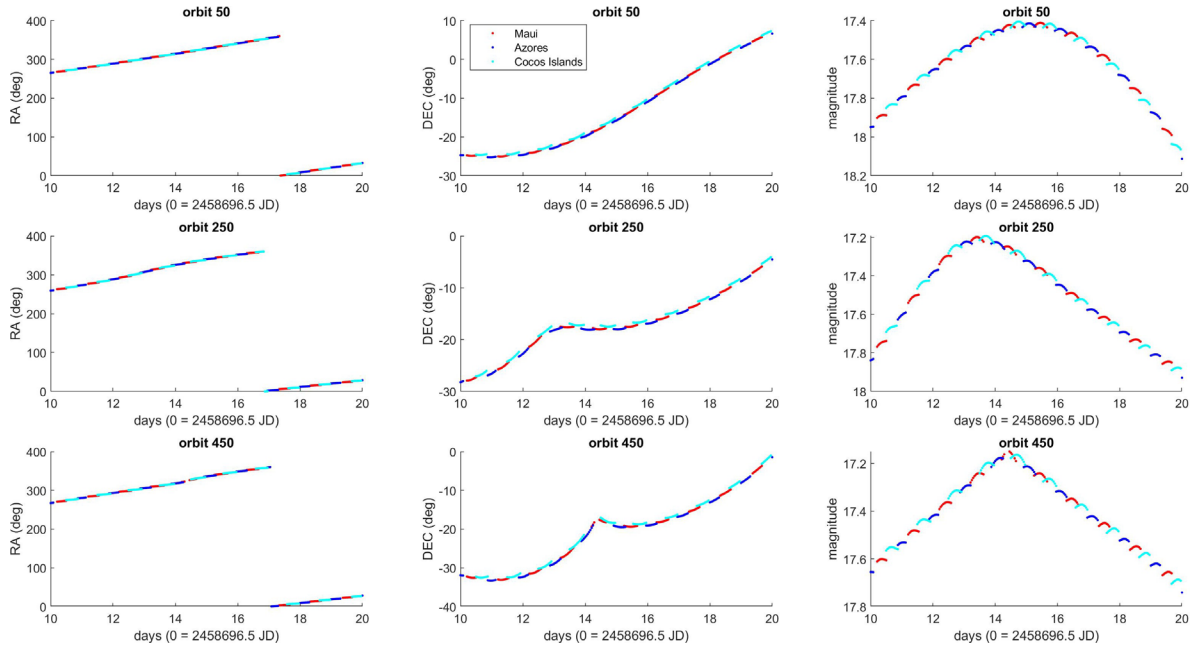


Figure 7. Zoomed-in RA/DEC and magnitude observations over only 10 days for diffuse spheres in HS2 orbits 50, 250, and 450 (red: Maui, blue: Azores, cyan: Cocos Islands).

Visible in Fig. 7, the individual colored “segments” correspond to nightly observations from each sensor. As is immediately evident, no single sensor can provide continuous coverage of the cislunar target; it is only with the collection of cooperative sensors that persistent tracking can be achieved (the minor mismatches are due to the slightly different perspectives offered by the different topocentric locations). Several conclusions can be drawn:

1. Target’s brightness approximately matches the solar phase angle of the Moon, i.e., full/new moon corresponds to peak/trough brightness.
2. Global extrema differ from cycle to cycle and correspond to changes in season.
3. Objects in cislunar orbits are fainter by approximately 5 magnitudes as compared to similar objects in GEO.
4. Considering a lunar exclusion zone, targets that remain near the Moon (in a relative motion sense) will be extremely challenging to see.
5. Multiple sensors and an asynchronous data collection strategy are required to maintain persistent coverage.
6. Objects in cislunar orbits do not generally travel in approximate planes.

At GEO, a single night of continuous observations is typically sufficient to build a full lightcurve for the entire orbit of a target. When the target is in a cislunar orbit, however, data is required to be collected over a considerably longer timeframe (a month or more⁵) to build that same “full lightcurve”. To compound the problem, while optimal solar phase angle alignments (producing glints) may last longer as compared to GEO, so will pessimal solar phase angle alignments (resulting in outages). In other words, with potentially many consecutive nights of null detections, the process of re-acquiring the same cislunar target after long gaps now must contend with larger uncertainties.

Figure 8 plots the AZ/EL as a function of time for the entire 122-day timespan of the scenario. Unlike for a GEO target, however, the cislunar target does not remain at a fixed azimuth (AZ) and elevation (EL) with respect to Earth-based sensors, but rather spans a wide range of values akin to the relative motion of the Moon and stars. Basically, in order to physically track cislunar objects, ground-based Earth sensors are required to exercise a wide range of slewing motion (that varies nightly) to keep the target in the field of view. Times of new moon are indicated with a vertical black line.

⁵ The precise amount of time is a function of the period of the target’s orbit.
DISTRIBUTION STATEMENT A: Approved for public release. Distribution unlimited.

Next, in order to test the dependence on the target's starting point, we vary the initial state of each target along their respective orbits (a particular periodic orbit is divided into 3 segments; the start of each segment thus corresponds to the choices for the target's starting point). Here, in Figure 9 and Figure 10, all sensors within a run – as parametrized by a different target starting point – are plotted with the same color; starting point 1 is red (effectively all of the previous analysis), starting point 2 is blue, and starting point 3 is cyan.

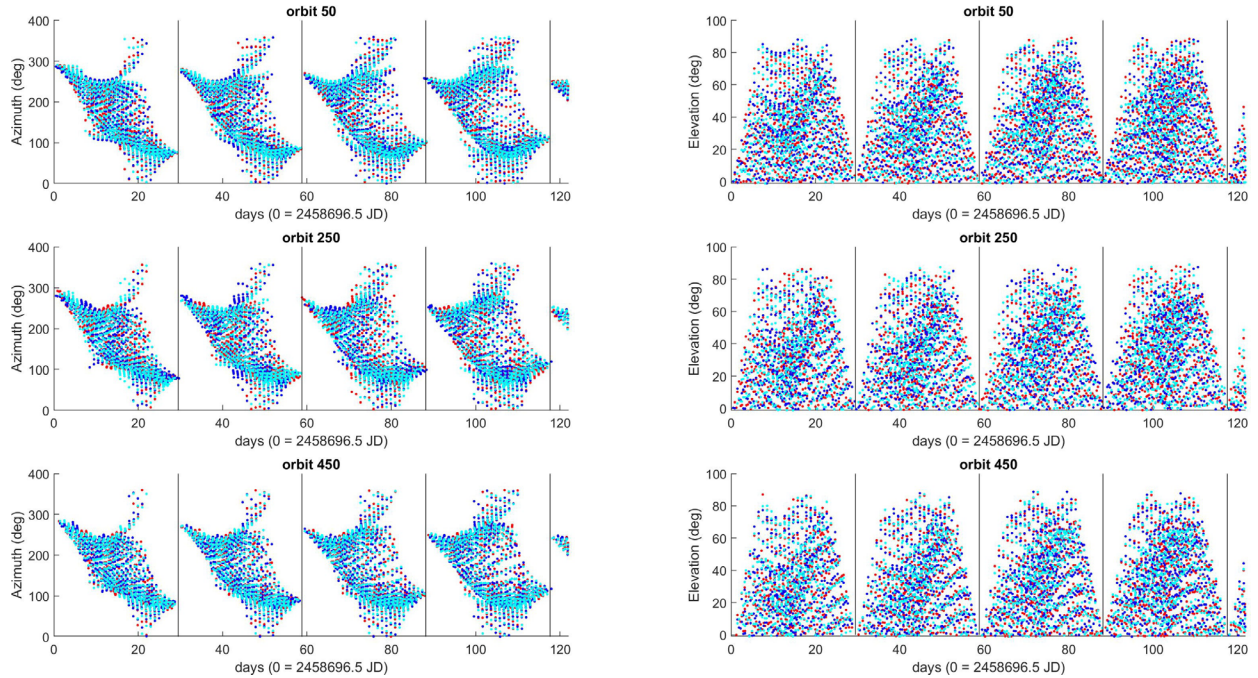


Figure 8. AZ/EL observations over the entire 122 days for diffuse spheres in HS2 orbits 50, 250, and 450 (red: Maui, blue: Azores, cyan: Cocos Islands).

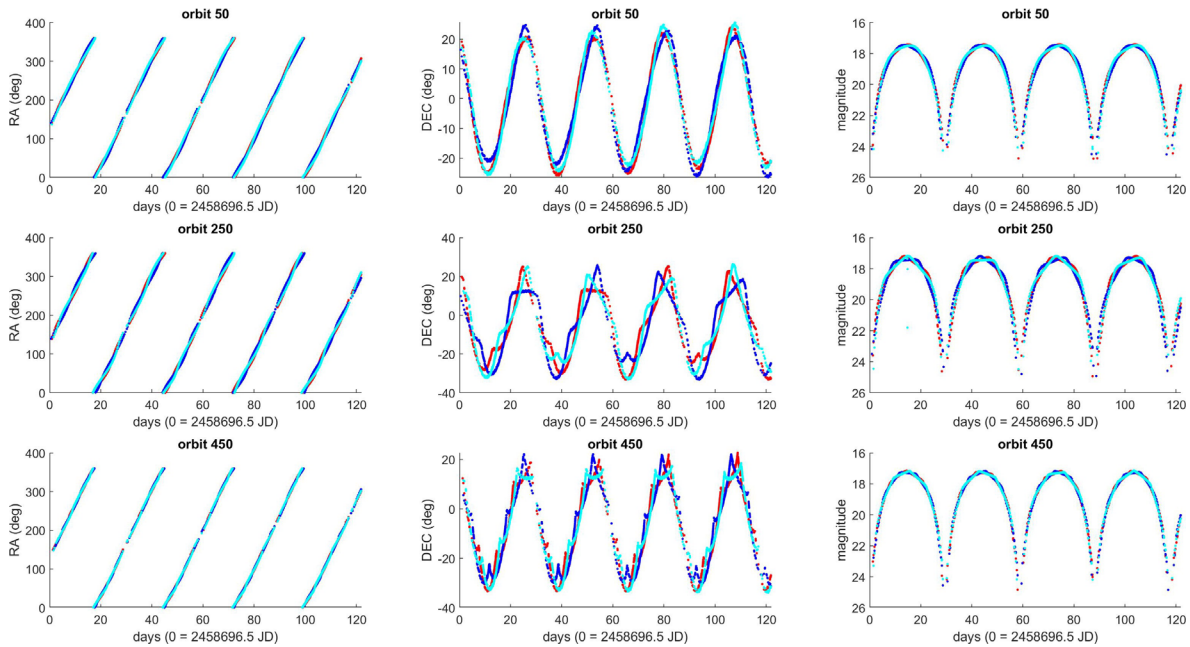


Figure 9. RA/DEC and magnitude observations over the entire 122 days for diffuse spheres in HS2 orbits 50, 250, and 450. Colors represent different starting points in the same periodic orbit.

DISTRIBUTION STATEMENT A: Approved for public release. Distribution unlimited.

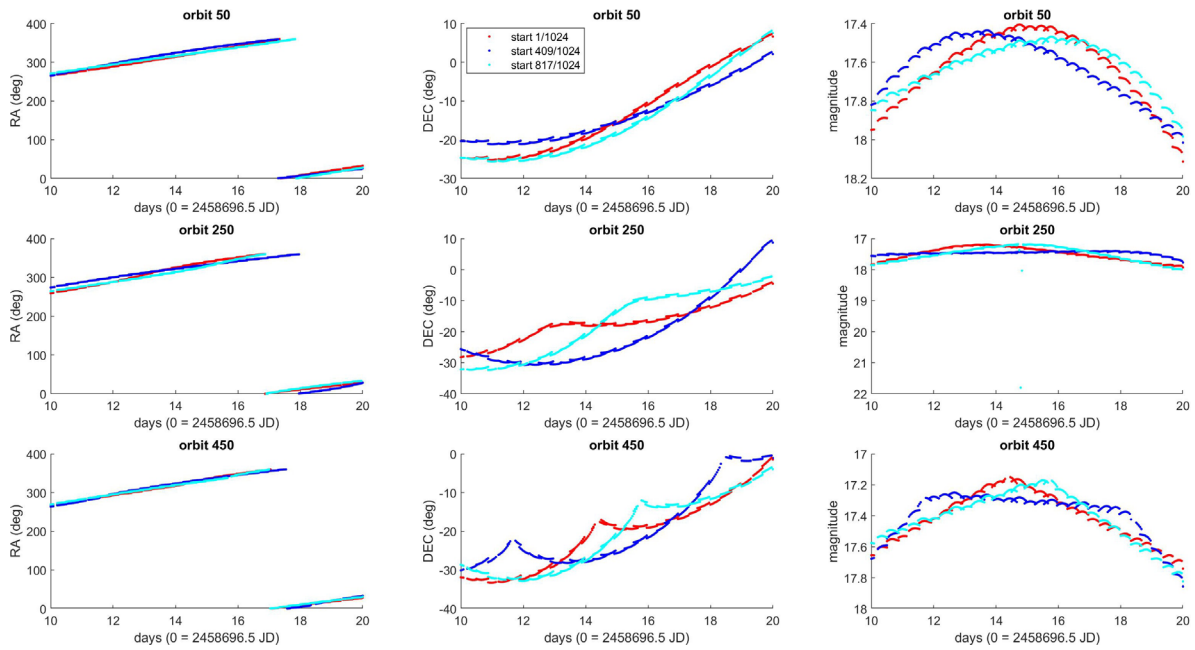


Figure 10. Zoomed-in RA/DEC and magnitude observations over only 10 days for diffuse spheres in HS2 orbits 50, 250, and 450. Colors represent different starting points in the same periodic orbit.

The lightcurves are roughly symmetric about zero solar phase angle for the Moon. The slight asymmetry in the lightcurve peaks is likely due to the difference in orbital geometry between the target and Moon. The astrometric features in each run seem to remain qualitatively the same but just shifted in time.

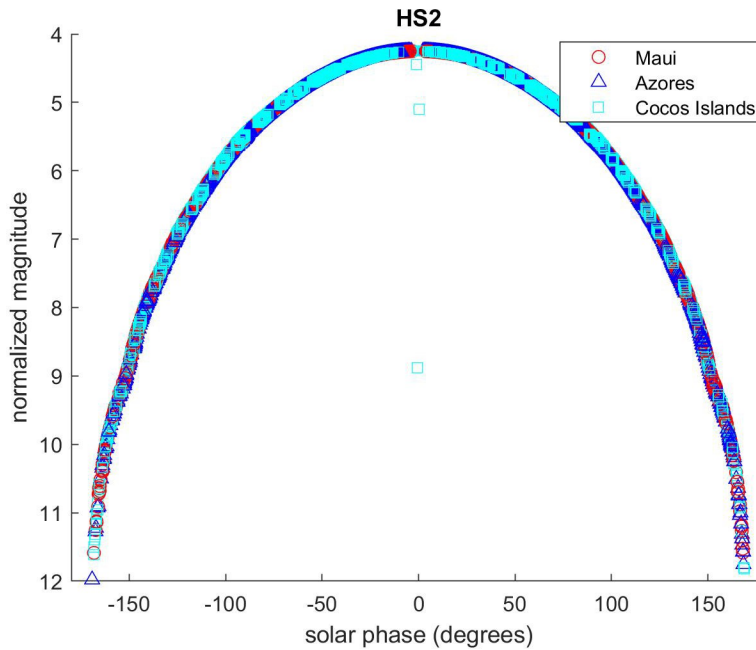


Figure 11. Normalized magnitude of the diffuse sphere vs. target's solar phase angle over 122 days for all 3 HS2 orbits and all 3 different starting points.

DISTRIBUTION STATEMENT A: Approved for public release. Distribution unlimited.

In order to account for these effects, we plot the magnitudes normalized to a constant range of 1000 km against the target's signed solar phase angle for all use cases. By convention, the sign of the solar phase angle is positive when the cross product of the Sun vector and sensor vector (as viewed from the object) has a positive inertial z-component and negative when it has a negative z-component. Not surprisingly, Figure 11 shows all lightcurves, irrespective of starting point, overlapping nearly exactly for the entire 122-day timespan (with slight differences due to the faceted approximation of the satellite). Note, the few points that do not fall on the curve occur when the target is within the Earth's or Moon's penumbral shadow during the observation (near zero solar phase angle). This alignment suggests that the timing of the observation with respect to the starting point of the target in a particular periodic orbit does not seem to affect the sensing behavior.

4.2 Observables of Targets in H1* and H2 from Moon-based Sensors

Sensor setup: Basing is on the Moon. Two hypothetical optical sensors are chosen at the following selenographic sites:

- Optimal ($\eta = 0.0^\circ$, $\eta_t = 113.7881^\circ$)
- Pessimial ($\eta = 0.0^\circ$, $\eta_t = 180.0^\circ$)

The timeframe for the simulation is 122 days (01 Aug 2019 – 30 Nov 2019); each sensor's observation interval is set to 1 hour. Pristine (i.e., no added uncertainty) lightcurves are computed to include only observations that meet the visibility criteria. The exclusion zones are arbitrarily set at 5° for the Earth and 10° for the Sun.

Target setup: H1* (H1 family truncated to include only the orbits up to the W4W5 bifurcation point; i.e., HN1 and HS1), HN2, and HS2 are selected as the host elemental periodic orbit families. Three different orbits are sampled from our orbital data set: H1* orbit 50, HN2 orbit 100, and HS2 orbit 400. The various HN2 and HS2 orbital periods range from approximately 6.05 to 14.85 days, and H1* from approximately 7.84 to 12.13 days.

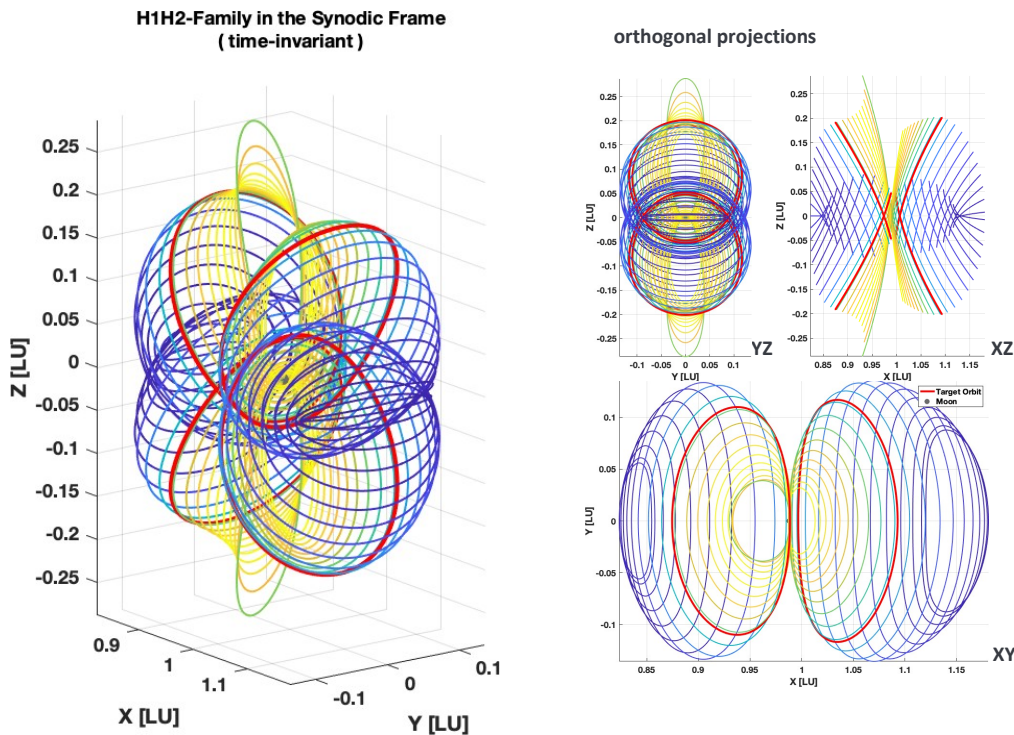


Figure 12. Host periodic orbit family set consisting of H1* (H1 family truncated to include only the orbits up to the W4W5 bifurcation point; i.e., HN1 and HS1), HN2, and HS2. Colors encode the orbital period (yellow: longest, blue: shortest), and red is used to highlight sample target orbits.

DISTRIBUTION STATEMENT A: Approved for public release. Distribution unlimited.

Figure 12 shows the manifolds for the $\mathcal{L}1$ and $\mathcal{L}2$ halo orbit families. Note, the full H1 family continues smoothly to eventually reach nearly $\mathcal{L}3$, but it is truncated here to include only those orbits that would be more relevant for lunar missions (i.e., are closer to the Moon). The color bar is a relative scale that maps to orbital period: yellow for longer and blue for shorter. The red orbits are included to distinguish sample orbits amongst the families.

The optimal/pessimal locations of the hypothetical selenographic sensors are determined by solving an optimization problem that maximizes the line-of-sight visibility to each coordinate in the periodic orbit host space. The problem formulation follows:

- Constraints
 - Azimuth: $0 \leq \alpha \leq 2\pi$
 - Co-elevation: $0 \leq \varrho \leq \pi/2$
- Parameters
 - Selenographic (Latitude, Longitude)⁶: $Z\eta, \eta; [$
 - Host orbits: $(\sigma(\tau), \tau)$
 - Other: $\eta_{<=}, !$
 - Selenographic Altitude
 - Boresight (Azimuth, Co-elevation)
 - FOV Axes (Major, Minor)
 - FOV Rotation Angle
 - FOV Shape
- Objective Function
 - Number of points in FOV: $J = \Sigma [\cos^{2\#}(\sigma(\tau) \cdot r)]$
- Optimization Problem
 - $Z\eta, \eta; [= \underset{?, ?\%}{\operatorname{argmax}} J(\eta, \eta; ; \eta_{<=}, !, \sigma(\tau), \tau)$

The complete solution space of the optimization problem is discretized in Figure 13 and overlaid on top of an image of the Moon. The optimal locations where the maximum number of ephemeris points are visible correspond to two areas in the xy-plane (of the Moon's orbit) near the in-track axis but shifted a few degrees towards the Earth-facing side. The suboptimal locations correspond to an annulus centered on the radial axis near the limb of the Earth-facing side. All other points are considered pessimal, including locations on the far side hemisphere of the Moon and a small patch inside the suboptimal annulus.

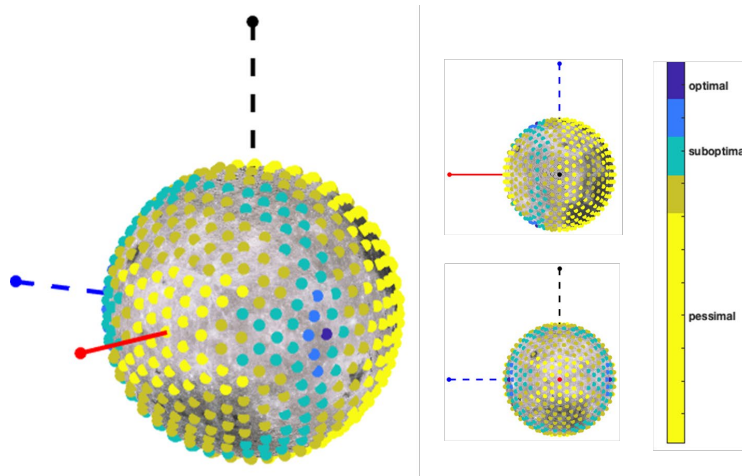


Figure 13. Results of optimizing lunar sensor placements to view H1* and H2 families. (red axis: toward Earth, blue axis: Moon's in-track direction, black axis: Moon's cross-track direction).

⁶ The coordinate system is not strictly aligned to the equatorial plane of the Moon but rather is aligned to the Moon's orbital plane about the Earth, with the origin centered at the Moon.

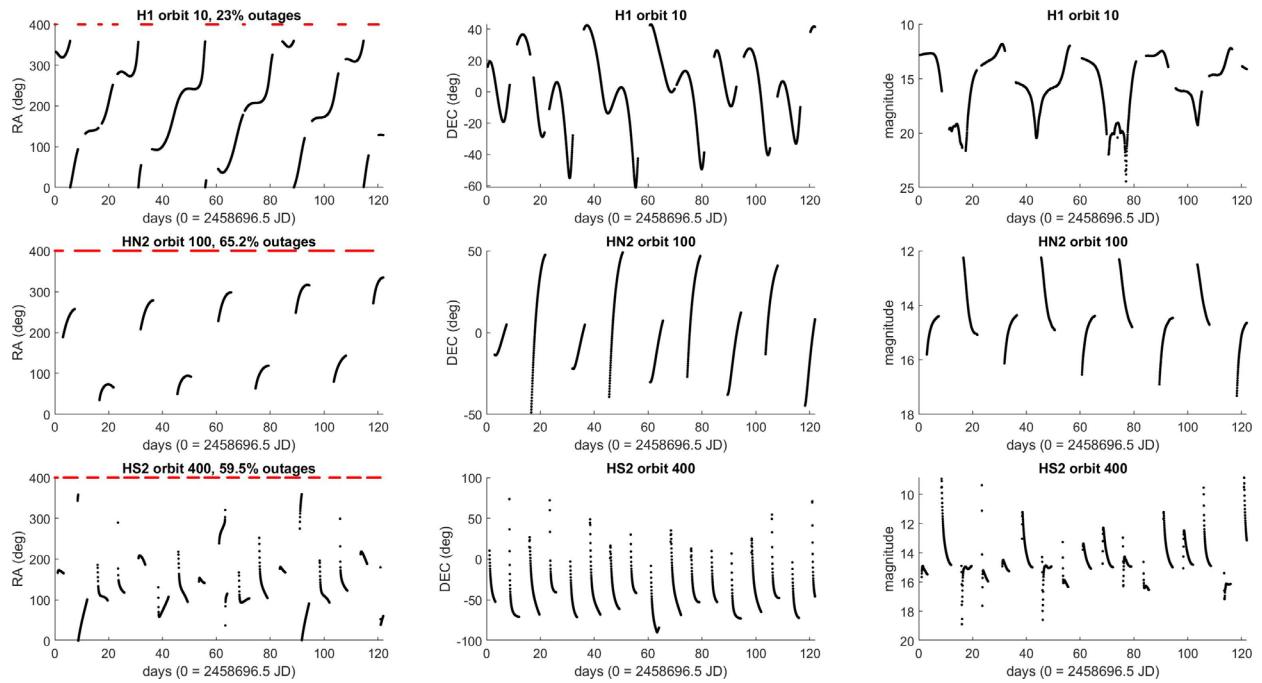


Figure 14. RA/DEC and magnitude observations over 122 days for diffuse spheres in H1 orbit 10, HN2 orbit 100, and HS2 orbit 400 for an optimal lunar sensor. Dashed red lines indicate outages.

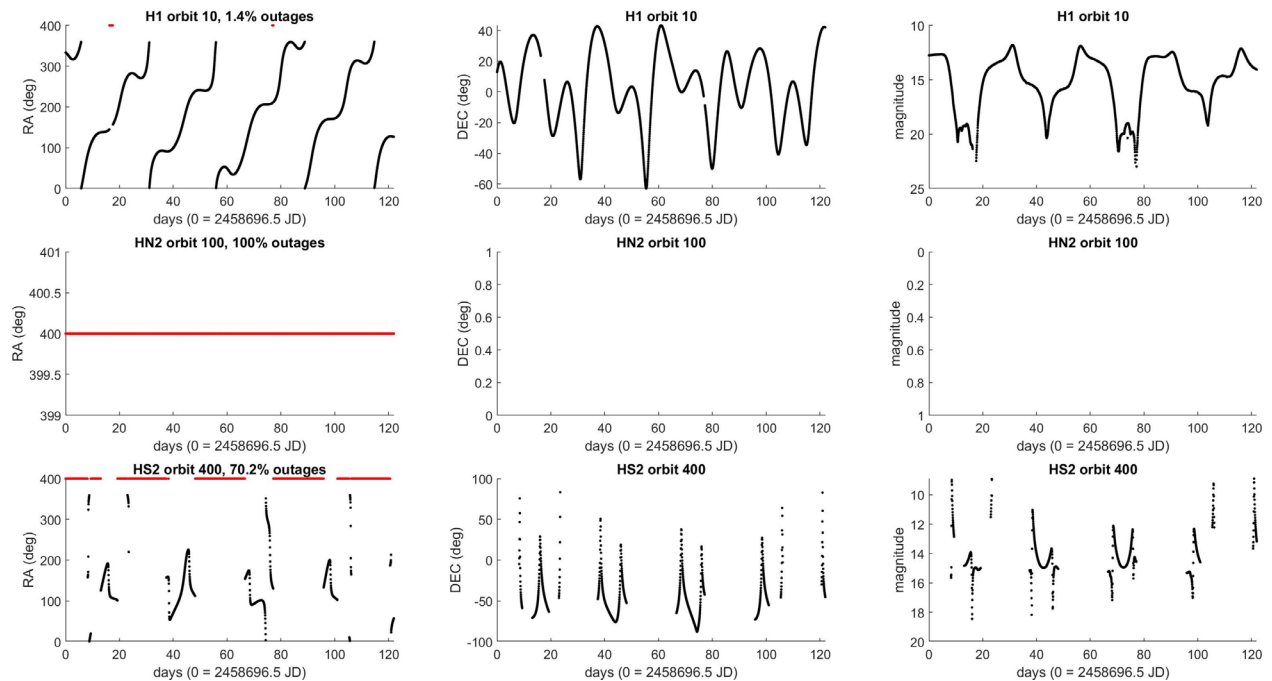


Figure 15. RA/DEC and magnitude observations over 122 days for diffuse spheres in H1 orbit 10, HN2 orbit 100, and HS2 orbit 400 for a pessimal lunar sensor. Dashed red lines indicate outages.

Figure 14 and Figure 15 plot Forge-derived observations of the diffuse sphere use case for two lunar sensors: (1) an optimal point ($\eta_i = 0^\circ$, $\eta_j = 113.7881^\circ$) and (2) a pessimal point ($\eta_i = 0^\circ$, $\eta_j = 180^\circ$). These two locations are chosen to provide a stark contrast when showing coverage from each sensor. In both cases, the observation gaps or outages are highlighted in red (only in the RA plots) with the numeric percentage values given in the figure titles. Overall, as expected, the optimal location experiences less cumulative outages for the same timeframe as compared to the pessimal location. In fact, the pessimal location cannot ever see the HN2 orbit 100 (due to the Moon being tidally locked with the Earth).

5. SUMMARY AND FUTURE WORK

This survey paper focuses on the sensor's astrometric and photometric responses to targets in cislunar space. A goal of this study is to provide some deeper intuition on how to inform cislunar sensor architecture designs. For this initial investigation we constrain the host target orbits to be the set of 31 elemental periodic orbits (Doedel et al., 2007) and a notional set of sensors to include 3 ground-based Earth and 2 Moon sensors. One outcome of this work is the actual data set that was generated: a large sampling (16,252,928 ephemeris records) of the elemental periodic orbit space. This data set is being used in other cislunar analyses, notably Martin et al., 2020.

Some challenges associated with observing cislunar targets:

- TLEs will no longer suffice
 - Cislunar orbits are often not representable by conic sections (i.e., non-Keplerian)
 - Cislunar orbits cannot be parameterized by a simple set of characteristics
- Detection is harder
 - Targets are fainter; longer distances will stress remote sensing capabilities
 - Targets are slower; longer time scales mean more observations are required to see significant fractions of orbits
- Tracking is harder
 - Targets no longer travel in approximate planes
 - Generally, the Earth is rotating faster than the orbits; a single ground-based sensor cannot maintain continuous coverage
 - May require asynchronous data collection strategies, impacting tasking and scheduling
- Estimation is harder
 - Orbits are very sensitive to initial conditions; dynamical systems models must be sufficiently accurate in order to predict and correct estimates of the state
 - Small perturbations can lead to wildly disproportionate outcomes (i.e., near chaos boundary)
 - Sparser data sampling affects association and correlation

To the last point, it merits further research to understand better exactly how initial orbit determination and orbit updates will be affected by various cislunar observation types, amounts, and cadences, all with/without maneuvers. The estimation engine itself may require a re-design (e.g., an ensemble filter of filters), as it remains to be seen if standard techniques can be effectively adapted for the cislunar problem.

Another natural extension within this sensor architecture study is to consider space-based assets as the observation platform. A similar analysis is being conducted to aid in orbit down-selection for AFRL's Cislunar Highway Patrol System (CHPS), using synthetic cislunar-to-cislunar and cislunar-to-lunar-transfer observations.

6. ACKNOWLEDGEMENTS

The authors wish to acknowledge insightful discussions with Dr. Phan Dao (AFRL/RV) and Dr. Anthony Dentamaro regarding the photometry of cislunar objects as compared to GEO.

7. REFERENCES

- Chow, C. Autonomous Interplanetary Constellation Design. *Ph.D. Dissertation*, University of Southern California, Los Angeles, CA, 2012.
- Doedel, E., Romanov, V., Paffenroth, R., Keller, H., Dichmann, D., Galan-Vioque, J., and A. Vanderbauwhede. Elemental Periodic Orbits Associated with the Libration Points in the Circular Restricted 3-body Problem. *International Journal of Bifurcation and Chaos*, 17(8):2625-2677, 2007.
- Keller, H. Numerical Solution of Bifurcation and Nonlinear Eigenvalue Problems. *Applications of Bifurcation Theory*, pp. 359-384, 1977.
- Martin, G., Wetterer, C.J., Lau, J., Toner, N., Chow, C.C., and P. Dao. Cislunar Periodic Orbit Family Classification from Astrometric and Photometric Observations using Machine-Learning. *The Advanced Maui Optical and Space Surveillance Technologies (AMOS) Conference*, Maui, HI, September 15-18, 2020.
- Vallado, D.A. and W.D. McClain. *Fundamentals of Astrodynamics and Applications*. 4th edition, New York: Springer, 2013.

8. APPENDIX

Table 3. A1 family's ranges of notable parameters and list of connection points.

Period	Jacobi Constant	Connects to
17.18 – 17.68 days	2.99 – 3.02	L1, V1

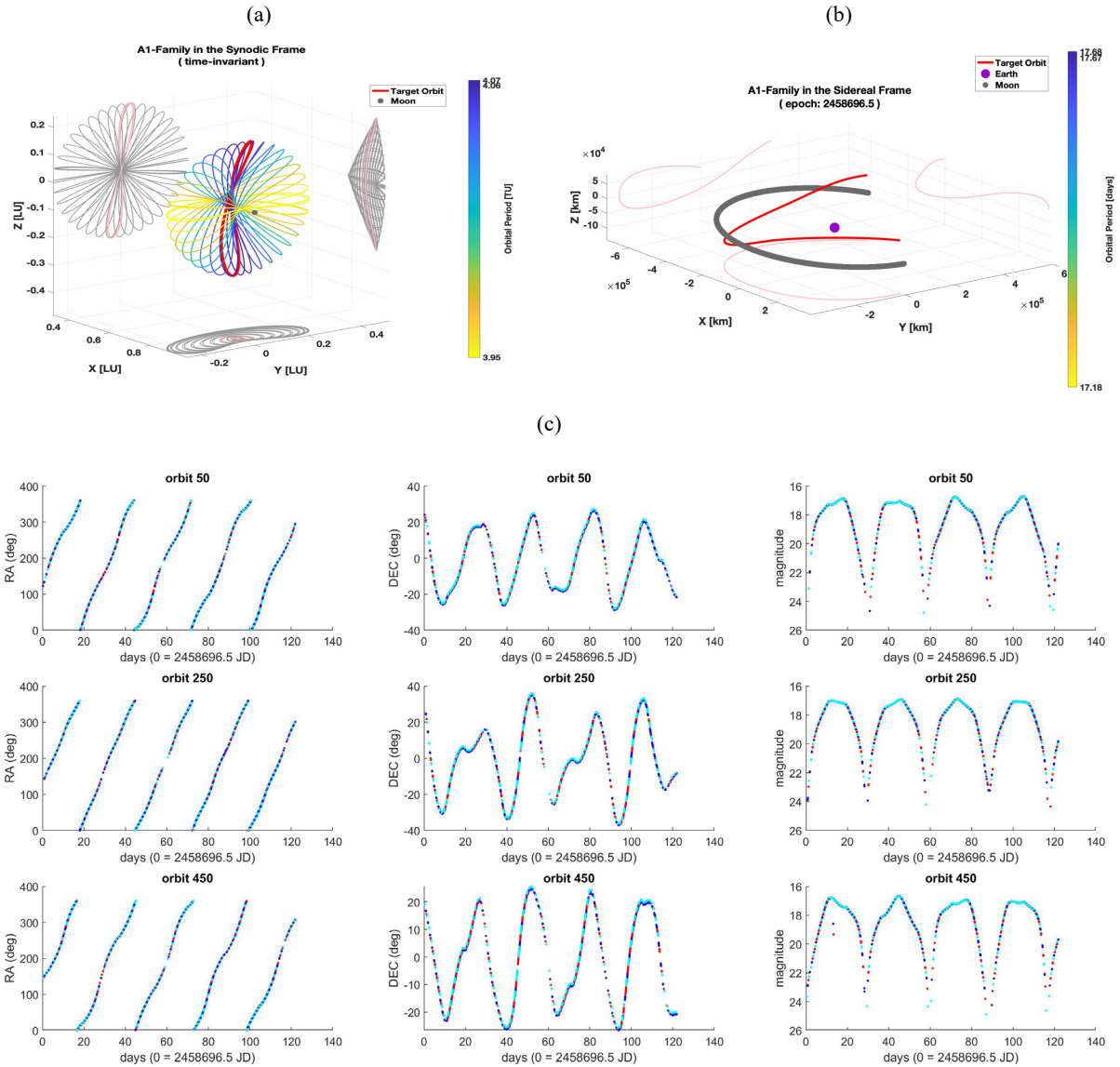


Figure 16. (a) A1 family in the synodic frame and (b) sample A1 target orbit in the sidereal frame for epoch 2019.08.01. (c) RA/DEC and magnitude observations over the entire 122 days for diffuse spheres in A1 orbits 50, 250, and 450 (red: Maui, blue: Azores, cyan: Cocos Islands).

Table 4. A2 family's ranges of notable parameters and list of connection points.

Period	Jacobi Constant	Connects to
18.74 – 19.23 days	2.97 – 3.01	L2, V2

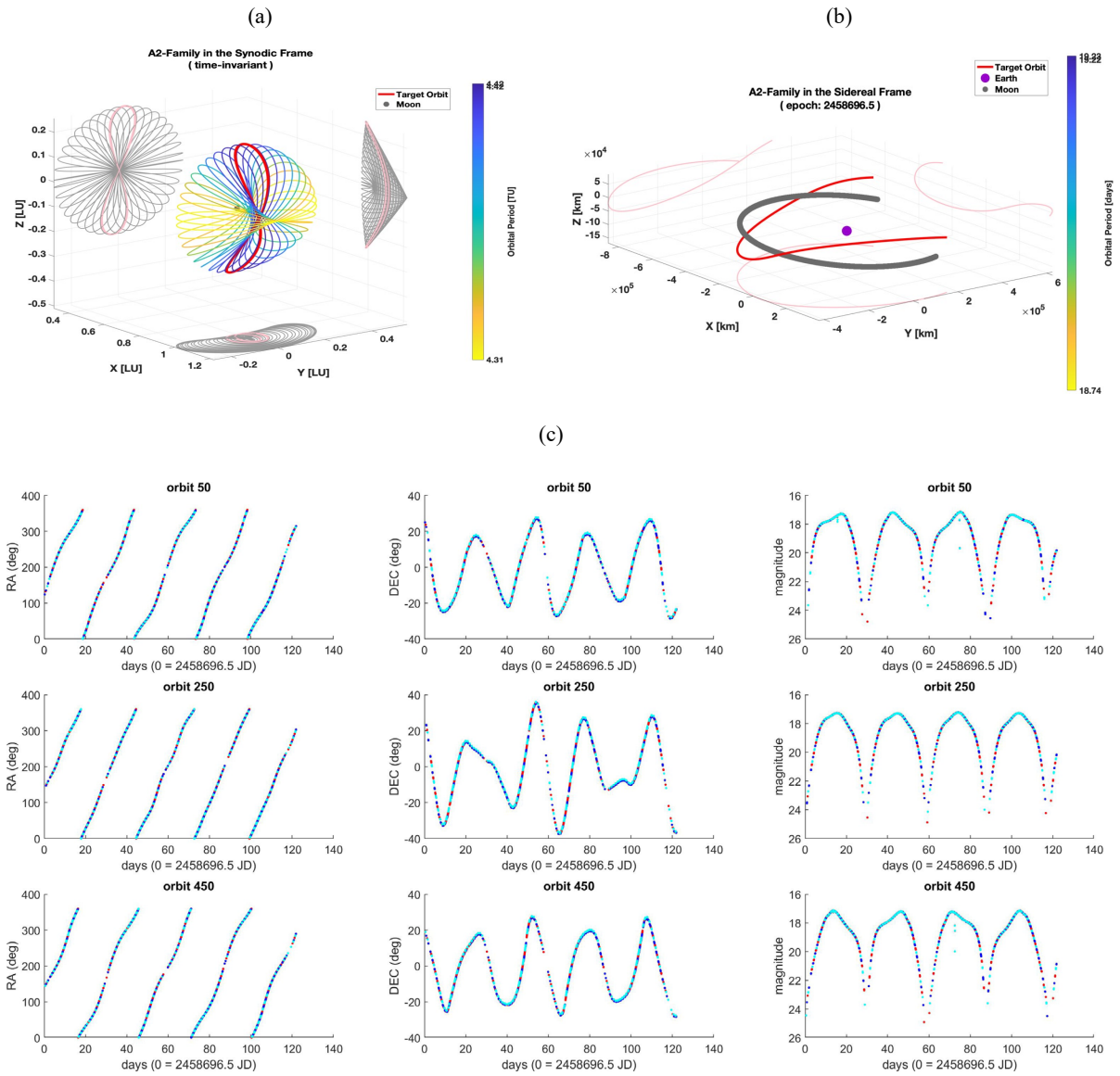


Figure 17. (a) A2 family in the synodic frame and (b) sample A2 target orbit in the sidereal frame for epoch 2019.08.01. (c) RA/DEC and magnitude observations over the entire 122 days for diffuse spheres in A2 orbits 50, 250, and 450 (red: Maui, blue: Azores, cyan: Cocos Islands).

Table 5. A3 family's ranges of notable parameters and list of connection points.

Period	Jacobi Constant	Connects to
27.23 – 27.25 days	0.03 – 1.86	L3, V3

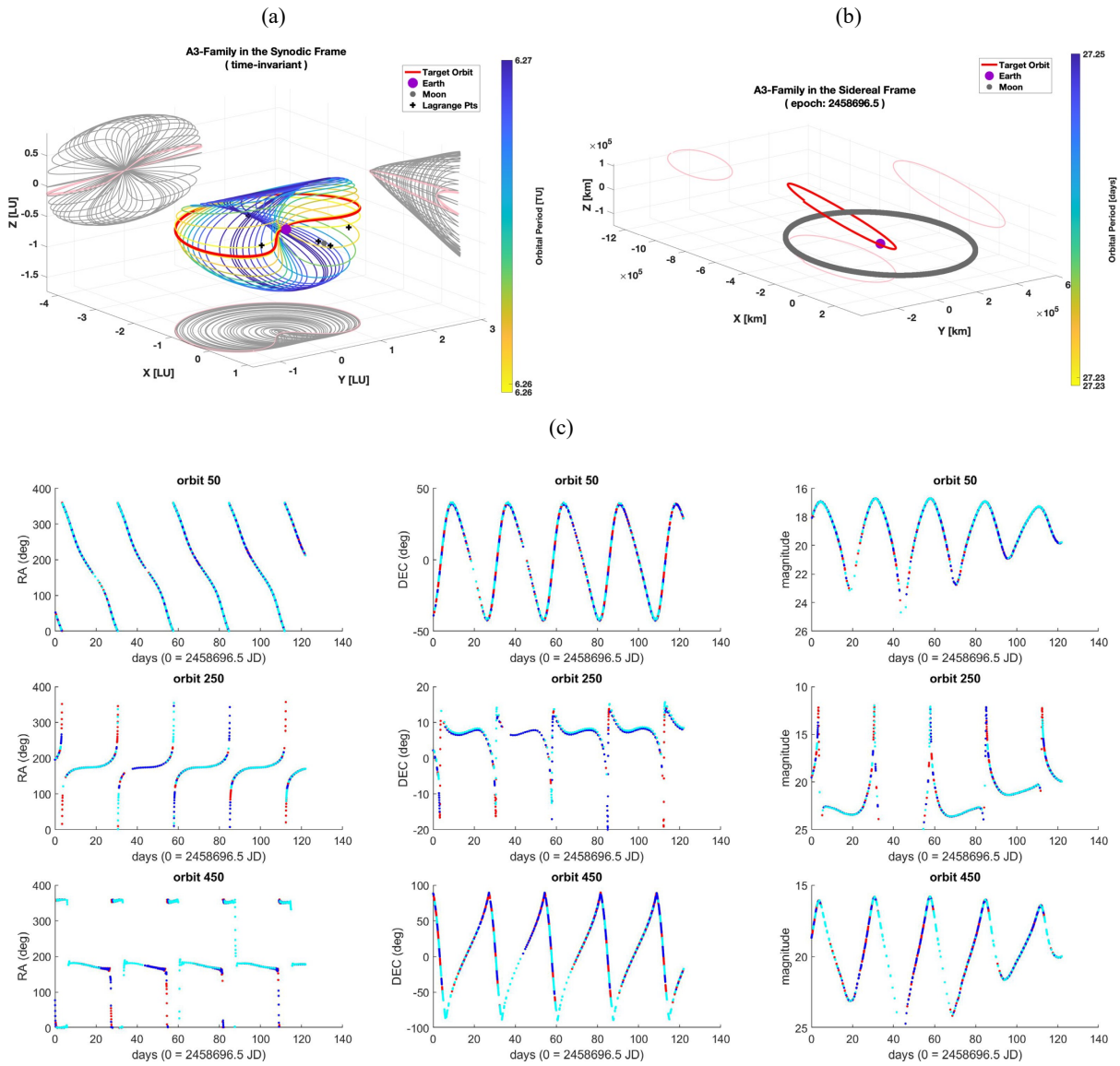


Figure 18. (a) A3 family in the synodic frame and (b) sample A3 target orbit in the sidereal frame for epoch 2019.08.01. (c) RA/DEC and magnitude observations over the entire 122 days for diffuse spheres in A3 orbits 50, 250, and 450 (red: Maui, blue: Azores, cyan: Cocos Islands).

Table 6. BN1 family's ranges of notable parameters and list of connection points.

Period	Jacobi Constant	Connects to
29.39 – 55.06 days	(-0.93) – 2.53	Moon, V1

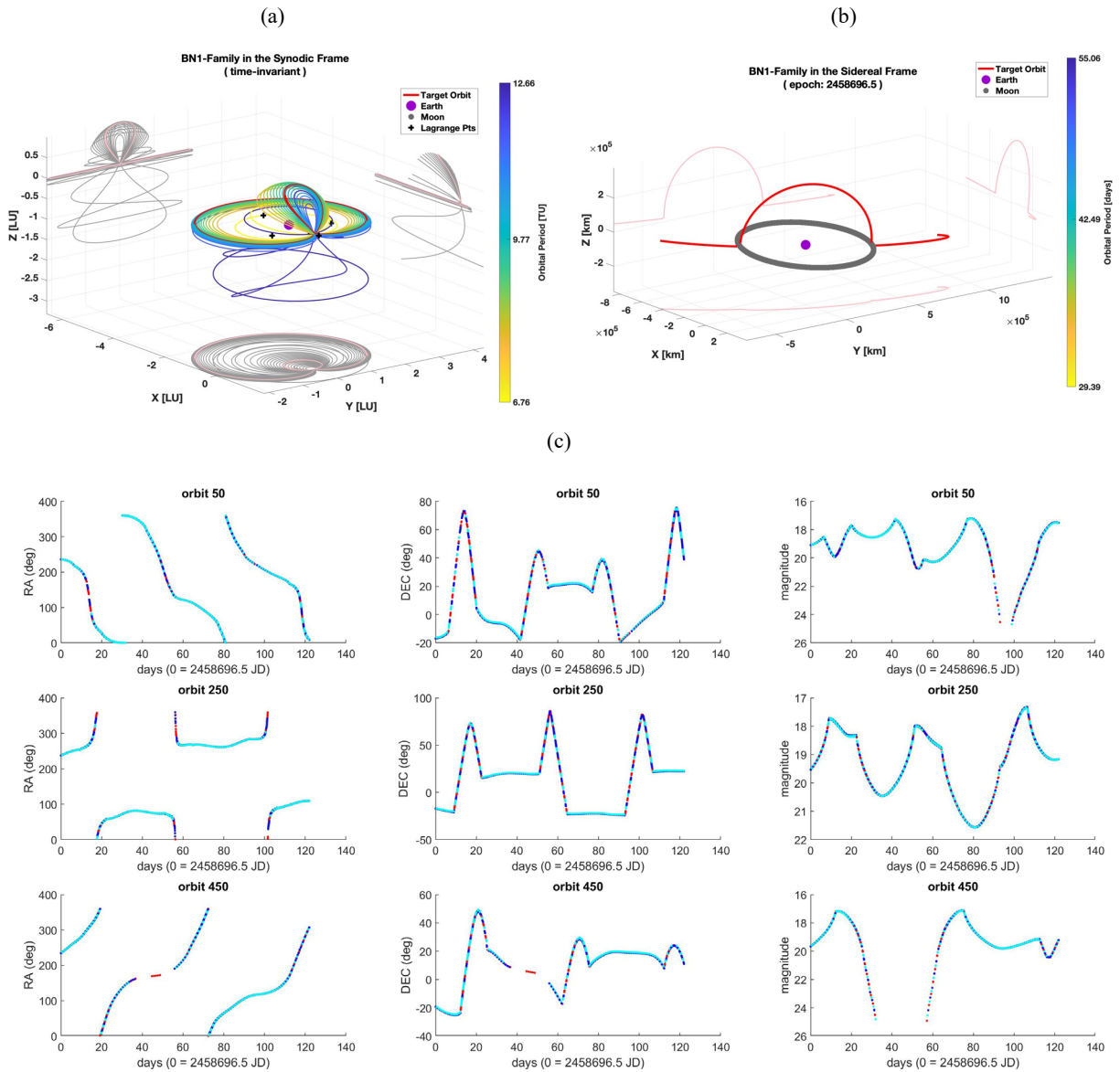


Figure 19. (a) BN1 family in the synodic frame and (b) sample BN1 target orbit in the sidereal frame for epoch 2019.08.01. (c) RA/DEC and magnitude observations over the entire 122 days for diffuse spheres in BN1 orbits 50, 250, and 450 (red: Maui, blue: Azores, cyan: Cocos Islands).

Table 7. BSI family's ranges of notable parameters and list of connection points.

Period	Jacobi Constant	Connects to
29.39 – 55.06 days	(-0.93) – 2.53	Moon, V1

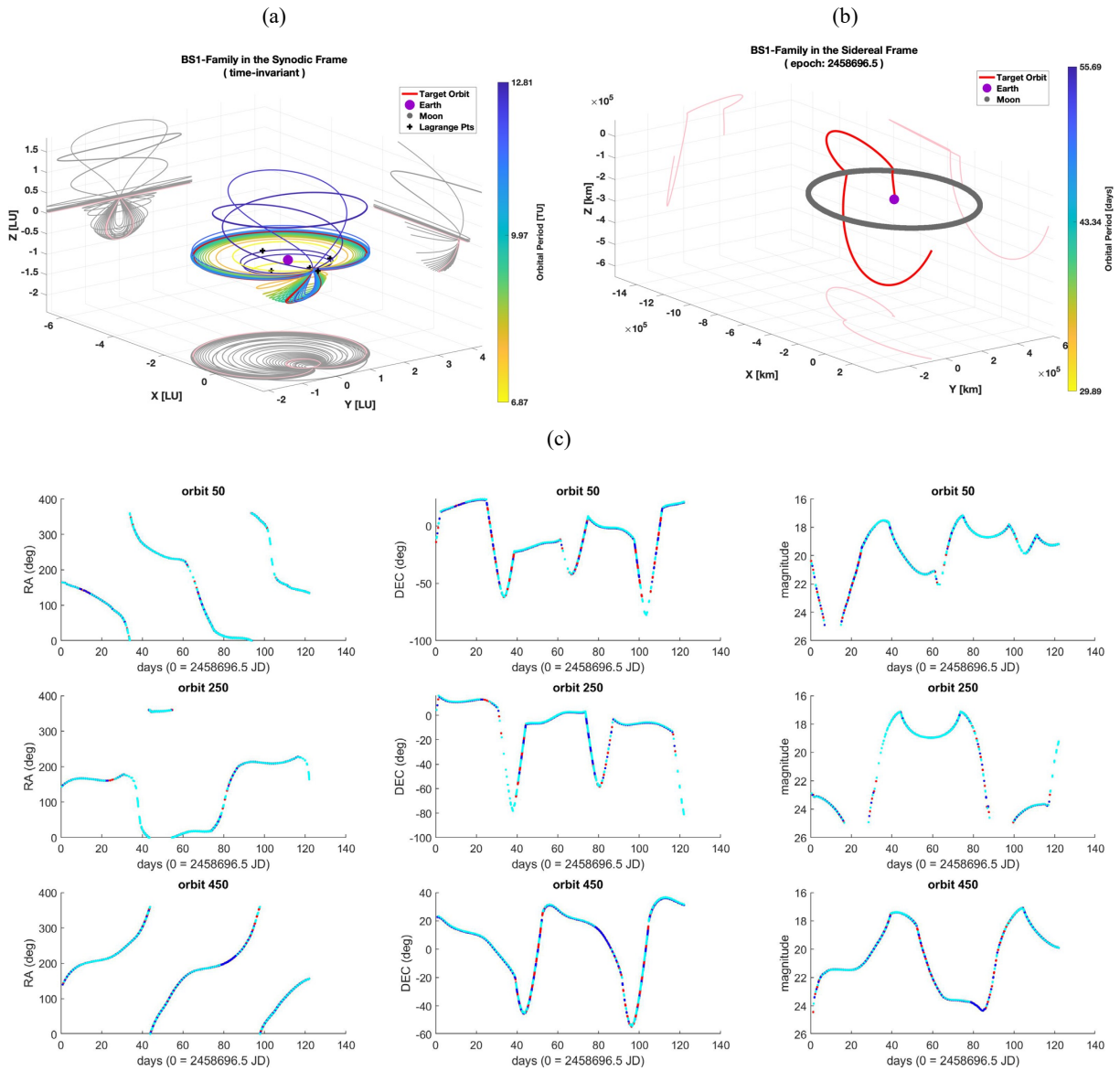


Figure 20. (a) BSI family in the synodic frame and (b) sample BSI target orbit in the sidereal frame for epoch 2019.08.01. (c) RA/DEC and magnitude observations over the entire 122 days for diffuse spheres in BSI orbits 50, 250, and 450 (red: Maui, blue: Azores, cyan: Cocos Islands).

Table 8. BN2 family's ranges of notable parameters and list of connection points.

Period	Jacobi Constant	Connects to
27.38 – 28.77 days	(-1.12) – 1.20	Earth, V2

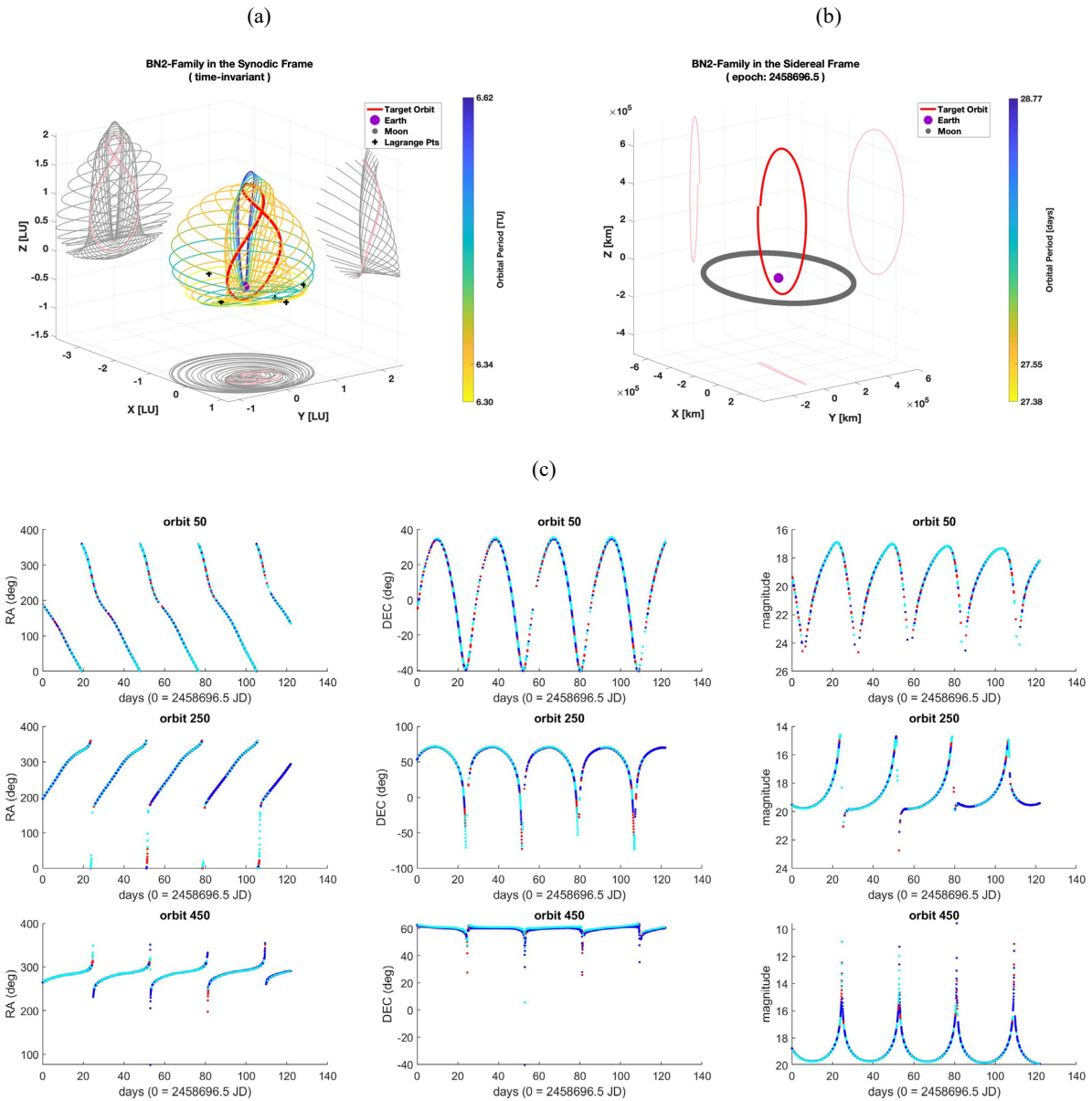


Figure 21. (a) BN2 family in the synodic frame and (b) sample BN2 target orbit in the sidereal frame for epoch 2019.08.01. (c) RA/DEC and magnitude observations over the entire 122 days for diffuse spheres in BN2 orbits 50, 250, and 450 (red: Maui, blue: Azores, cyan: Cocos Islands).

Table 9. BS2 family's ranges of notable parameters and list of connection points.

Period	Jacobi Constant	Connects to
27.38 – 28.77 days	(-1.12) – 1.20	Earth, V2

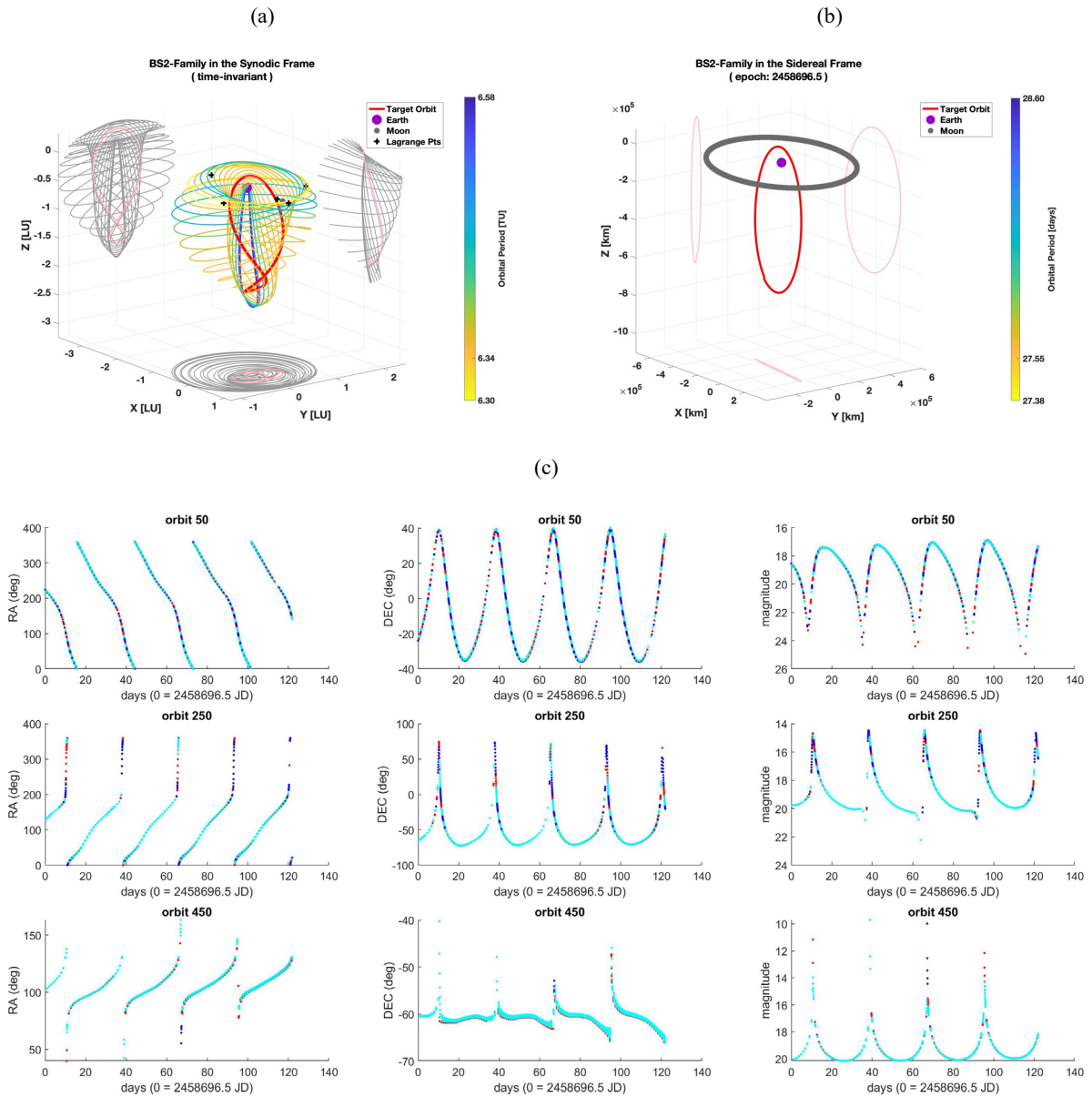


Figure 22. (a) BS2 family in the synodic frame and (b) sample BS2 target orbit in the sidereal frame for epoch 2019.08.01. (c) RA/DEC and magnitude observations over the entire 122 days for diffuse spheres in BS2 orbits 50, 250, and 450 (red: Maui, blue: Azores, cyan: Cocos Islands).

Table 10. B3 family's ranges of notable parameters and list of connection points.

Period	Jacobi Constant	Connects to
28.84 – 29.87 days	(-1.15) – (-1.09)	D1, V1

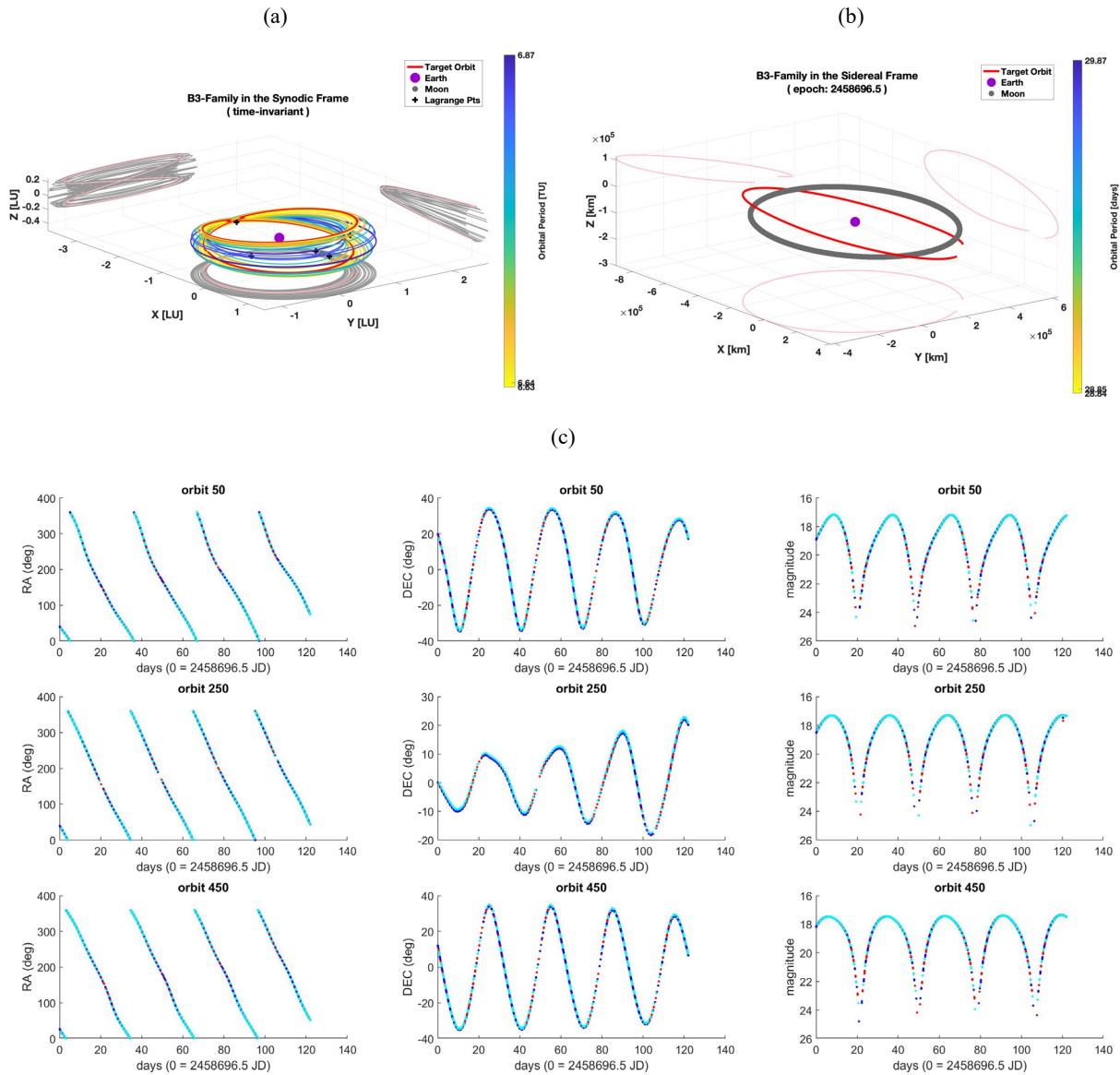


Figure 23. (a) B3 family in the synodic frame and (b) sample B3 target orbit in the sidereal frame for epoch 2019.08.01. (c) RA/DEC and magnitude observations over the entire 122 days for diffuse spheres in B3 orbits 50, 250, and 450 (red: Maui, blue: Azores, cyan: Cocos Islands).

Table 11. C1 family's ranges of notable parameters and list of connection points.

Period	Jacobi Constant	Connects to
27.61 – 45.00 days	(-0.89) – (-0.03)	V1

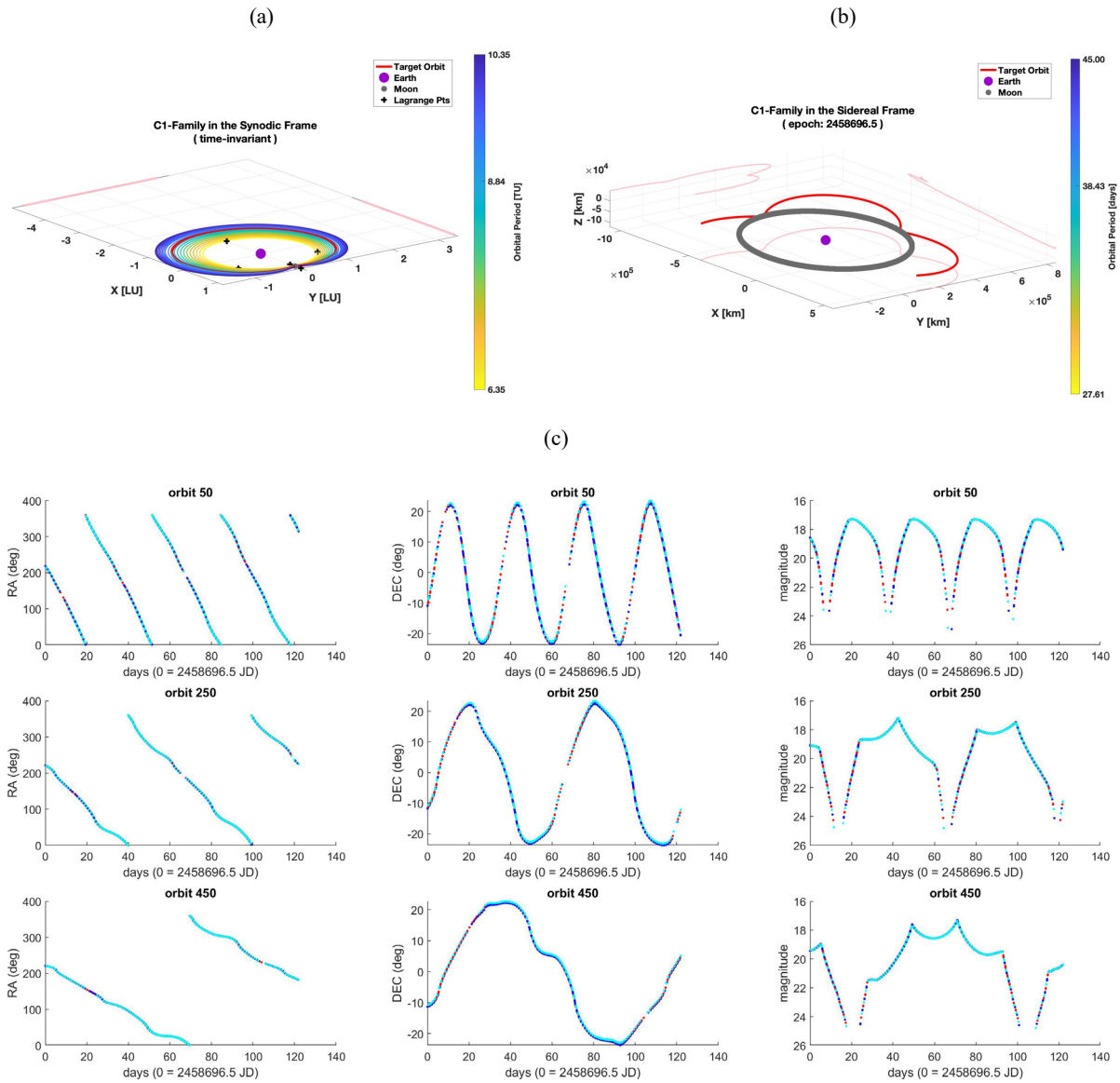


Figure 24. (a) C1 family in the synodic frame and (b) sample C1 target orbit in the sidereal frame for epoch 2019.08.01. (c) RA/DEC and magnitude observations over the entire 122 days for diffuse spheres in C1 orbits 50, 250, and 450 (red: Maui, blue: Azores, cyan: Cocos Islands).

Table 12. C2 family's ranges of notable parameters and list of connection points.

Period	Jacobi Constant	Connects to
30.47 – 50.76 days	(-4.53) – (-1.35)	H1, V2, V3

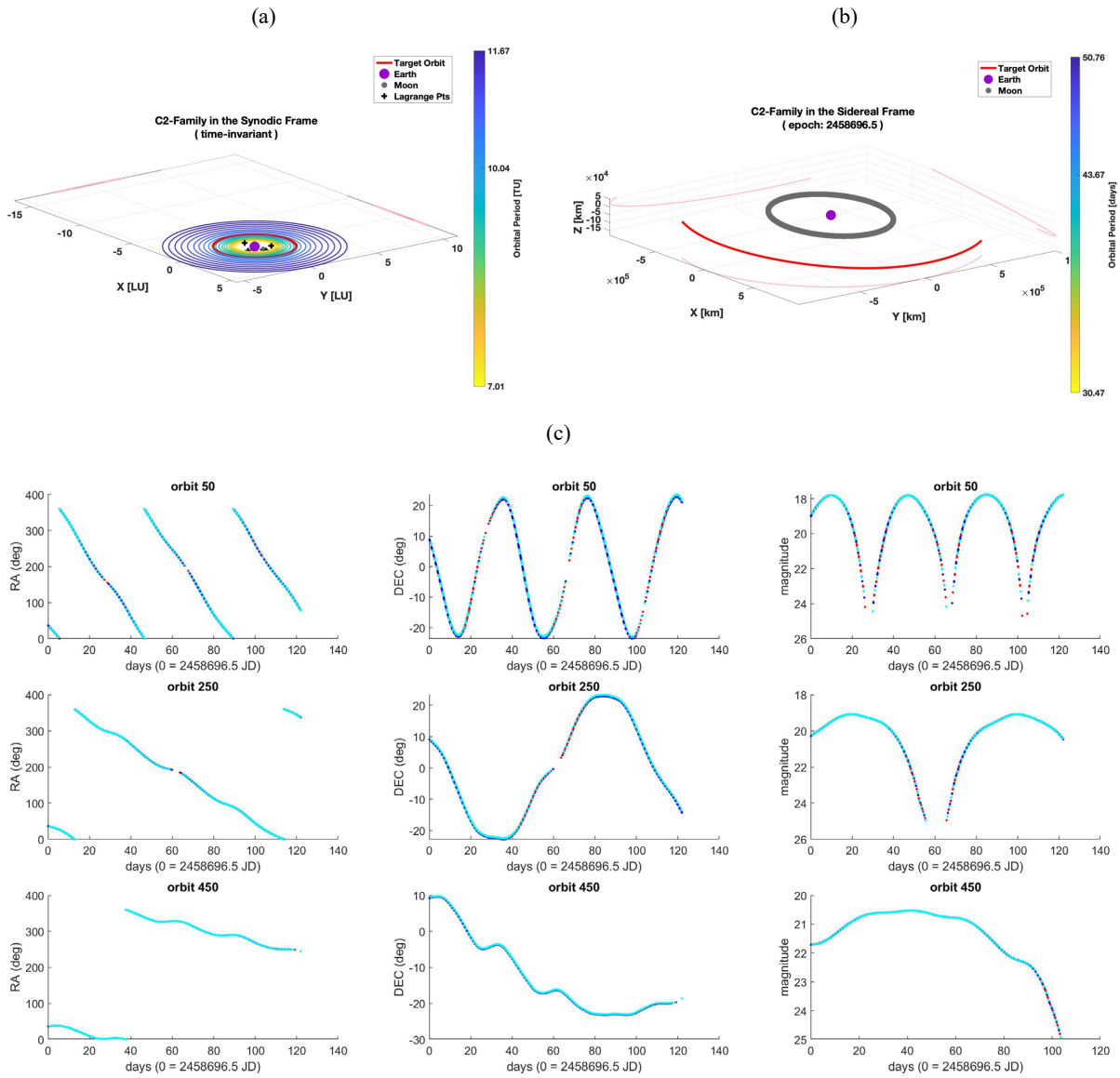


Figure 25. (a) C2 family in the synodic frame and (b) sample C2 target orbit in the sidereal frame for epoch 2019.08.01. (c) RA/DEC and magnitude observations over the entire 122 days for diffuse spheres in C2 orbits 50, 250, and 450 (red: Maui, blue: Azores, cyan: Cocos Islands).

Table 13. D1 family's ranges of notable parameters and list of connection points.

Period	Jacobi Constant	Connects to
30.08 – 67.17 days	(-1.41) – (2.46)	B3, C1, E1

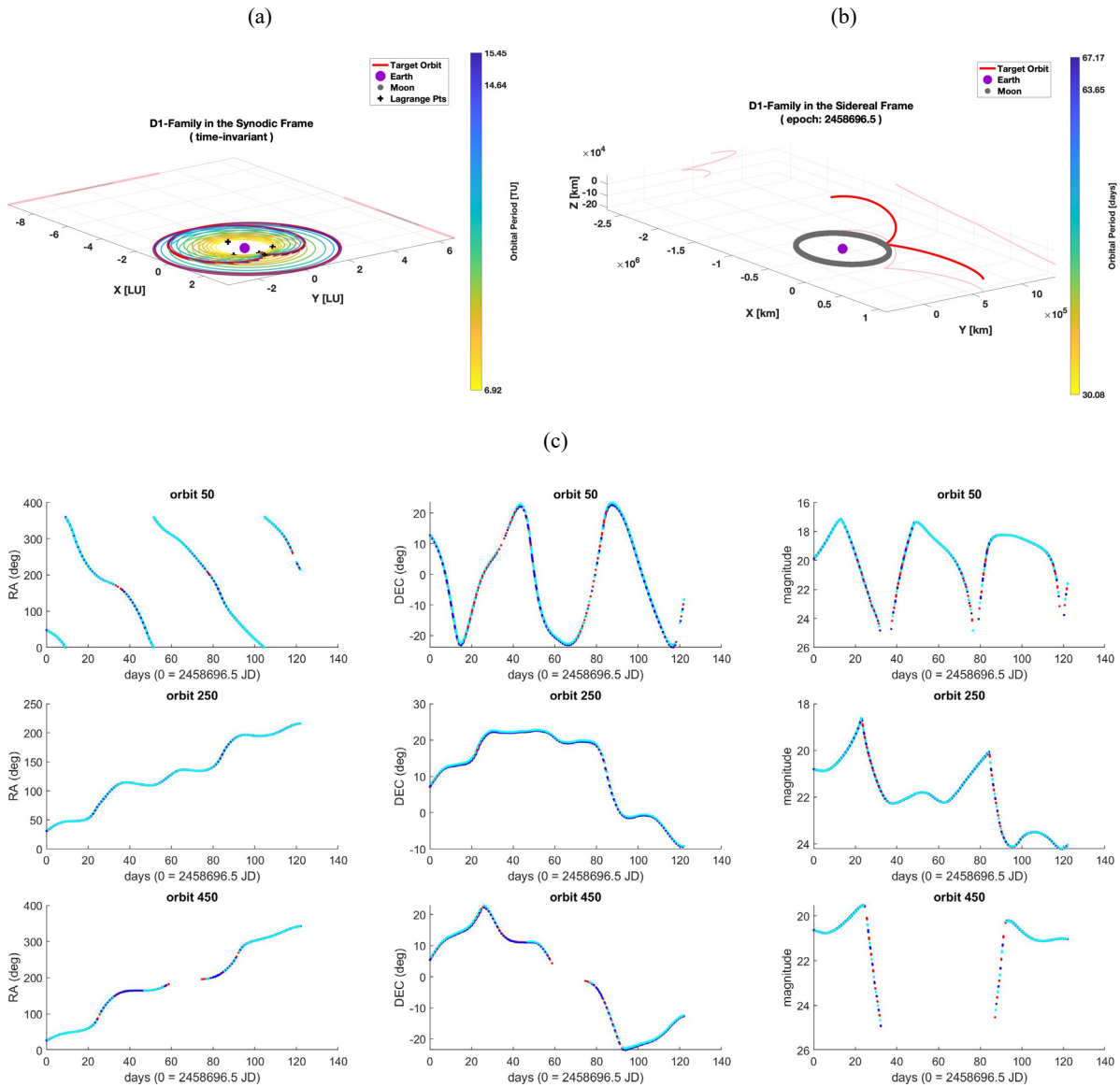


Figure 26. (a) D1 family in the synodic frame and (b) sample D1 target orbit in the sidereal frame for epoch 2019.08.01. (c) RA/DEC and magnitude observations over the entire 122 days for diffuse spheres in D1 orbits 50, 250, and 450 (red: Maui, blue: Azores, cyan: Cocos Islands).

Table 14. EN1 family's ranges of notable parameters and list of connection points.

Period	Jacobi Constant	Connects to
40.00 – 40.90 days	(-1.30) – (2.67)	D1

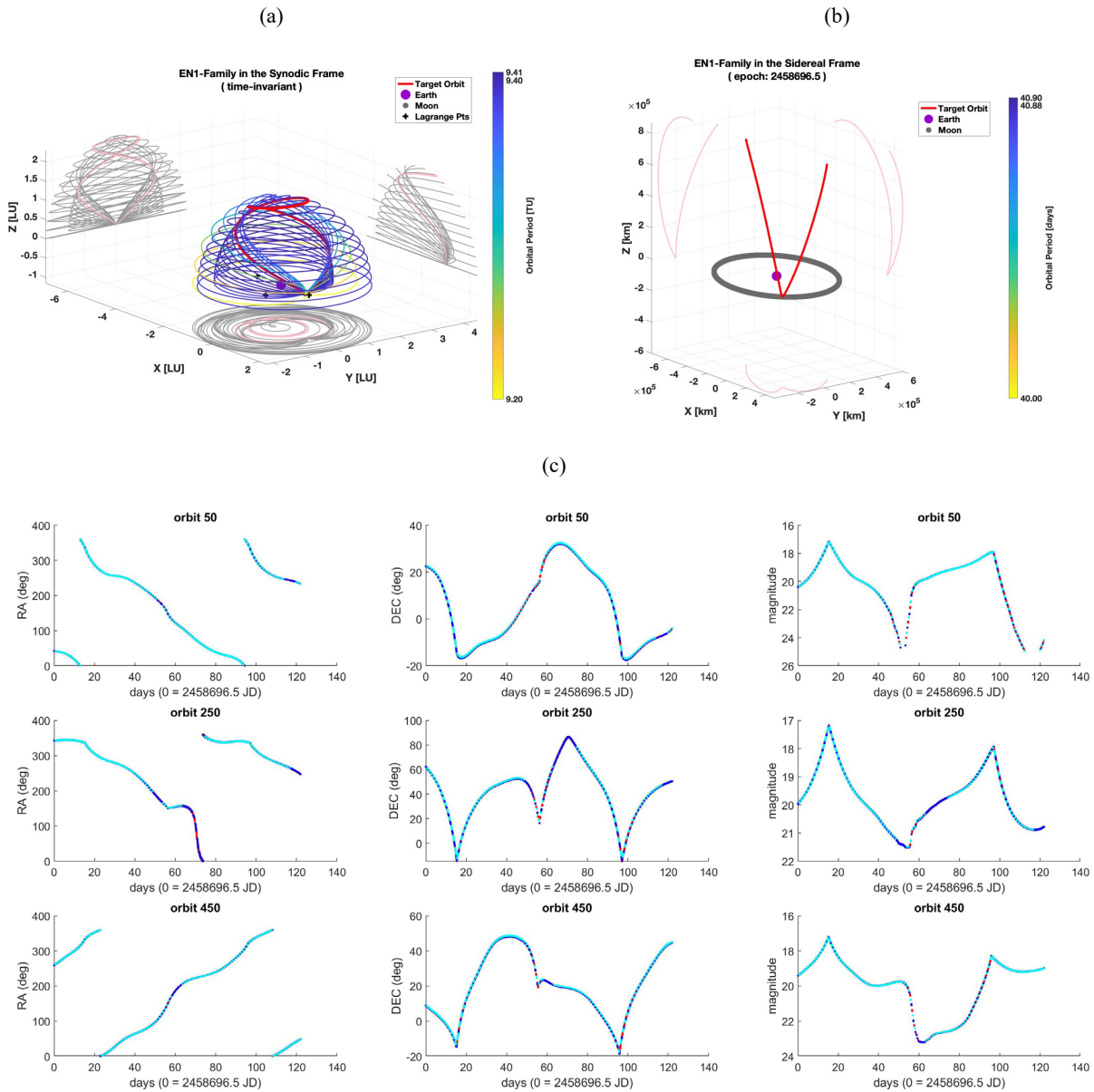


Figure 27. (a) EN1 family in the synodic frame and (b) sample EN1 target orbit in the sidereal frame for epoch 2019.08.01. (c) RA/DEC and magnitude observations over the entire 122 days for diffuse spheres in EN1 orbits 50, 250, and 450 (red: Maui, blue: Azores, cyan: Cocos Islands).

Table 15. ES1 family's ranges of notable parameters and list of connection points.

Period	Jacobi Constant	Connects to
40.00 – 40.90 days	(-1.30) – (2.67)	D1

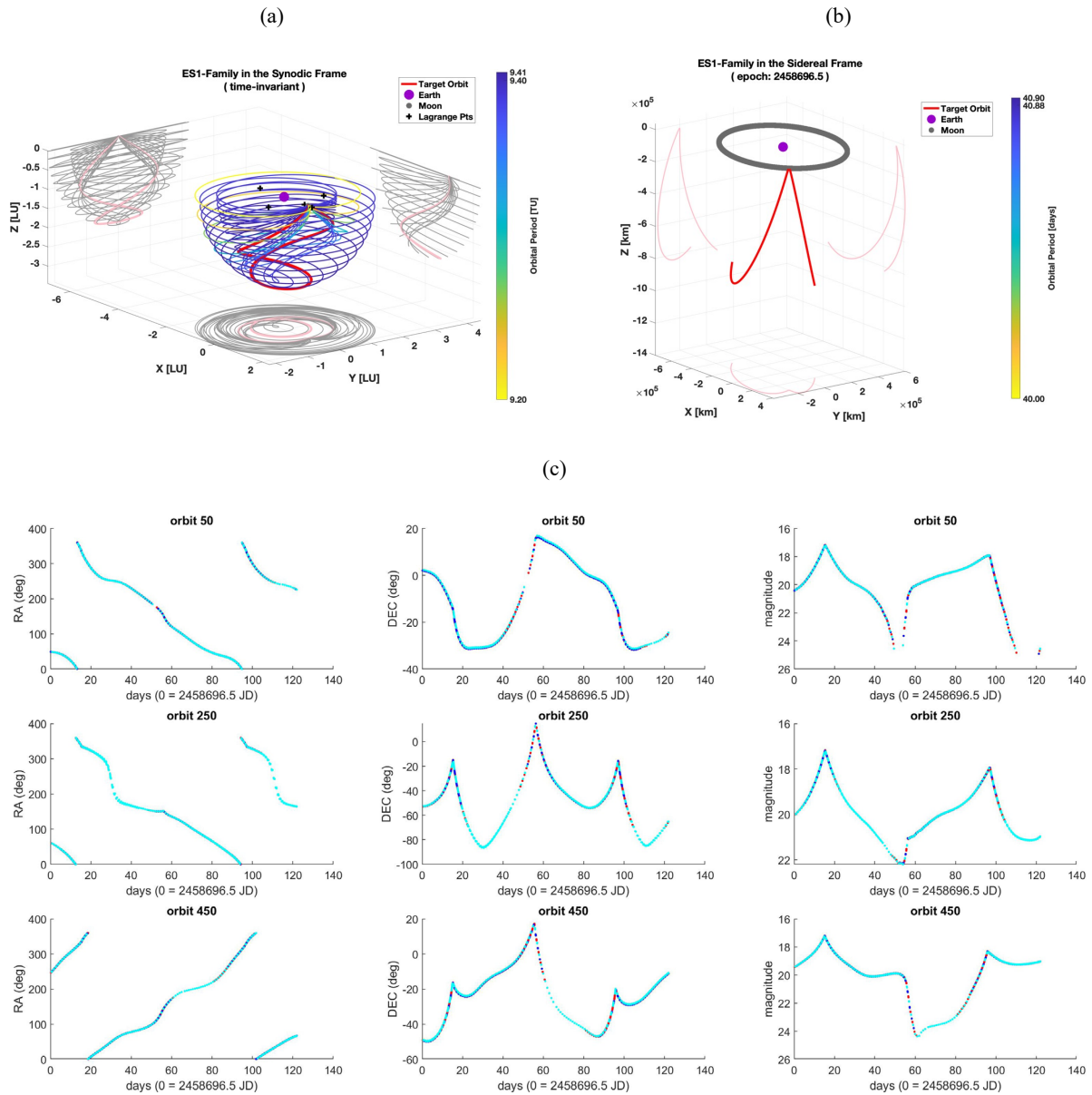


Figure 28. (a) ES1 family in the synodic frame and (b) sample ES1 target orbit in the sidereal frame for epoch 2019.08.01. (c) RA/DEC and magnitude observations over the entire 122 days for diffuse spheres in ES1 orbits 50, 250, and 450 (red: Maui, blue: Azores, cyan: Cocos Islands).

Table 16. H1 family's ranges of notable parameters and list of connection points.

Period	Jacobi Constant	Connects to
7.84 – 13.58 days	2.94 – 3.17	C2, L1, W4W5

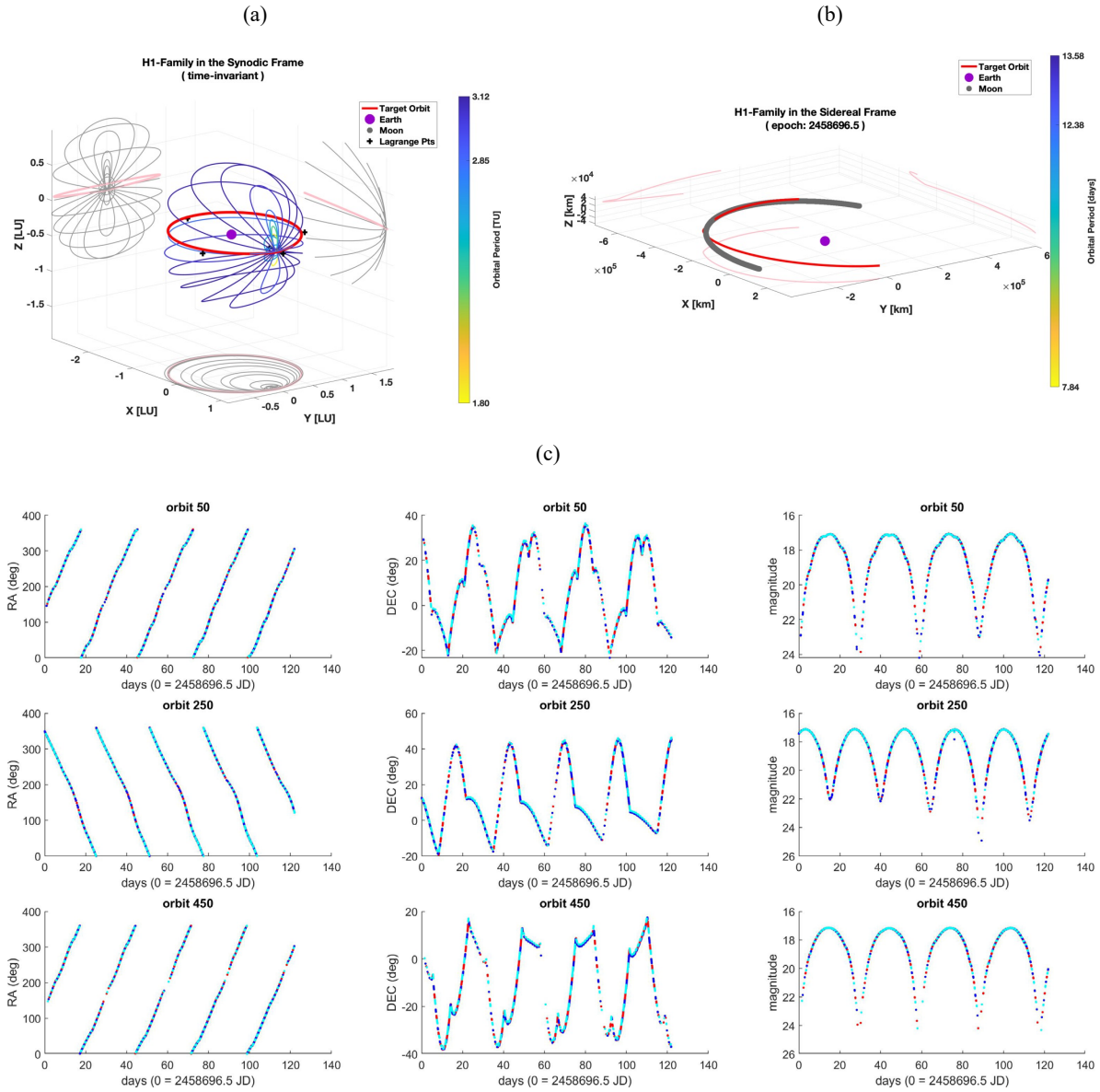


Figure 29. (a) H1 family in the synodic frame and (b) sample H1 target orbit in the sidereal frame for epoch 2019.08.01. (c) RA/DEC and magnitude observations over the entire 122 days for diffuse spheres in H1 orbits 50, 250, and 450 (red: Maui, blue: Azores, cyan: Cocos Islands).

Table 17. HN2 family's ranges of notable parameters and list of connection points.

Period	Jacobi Constant	Connects to
6.05 – 14.85 days	3.02 – 3.15	Moon, L2

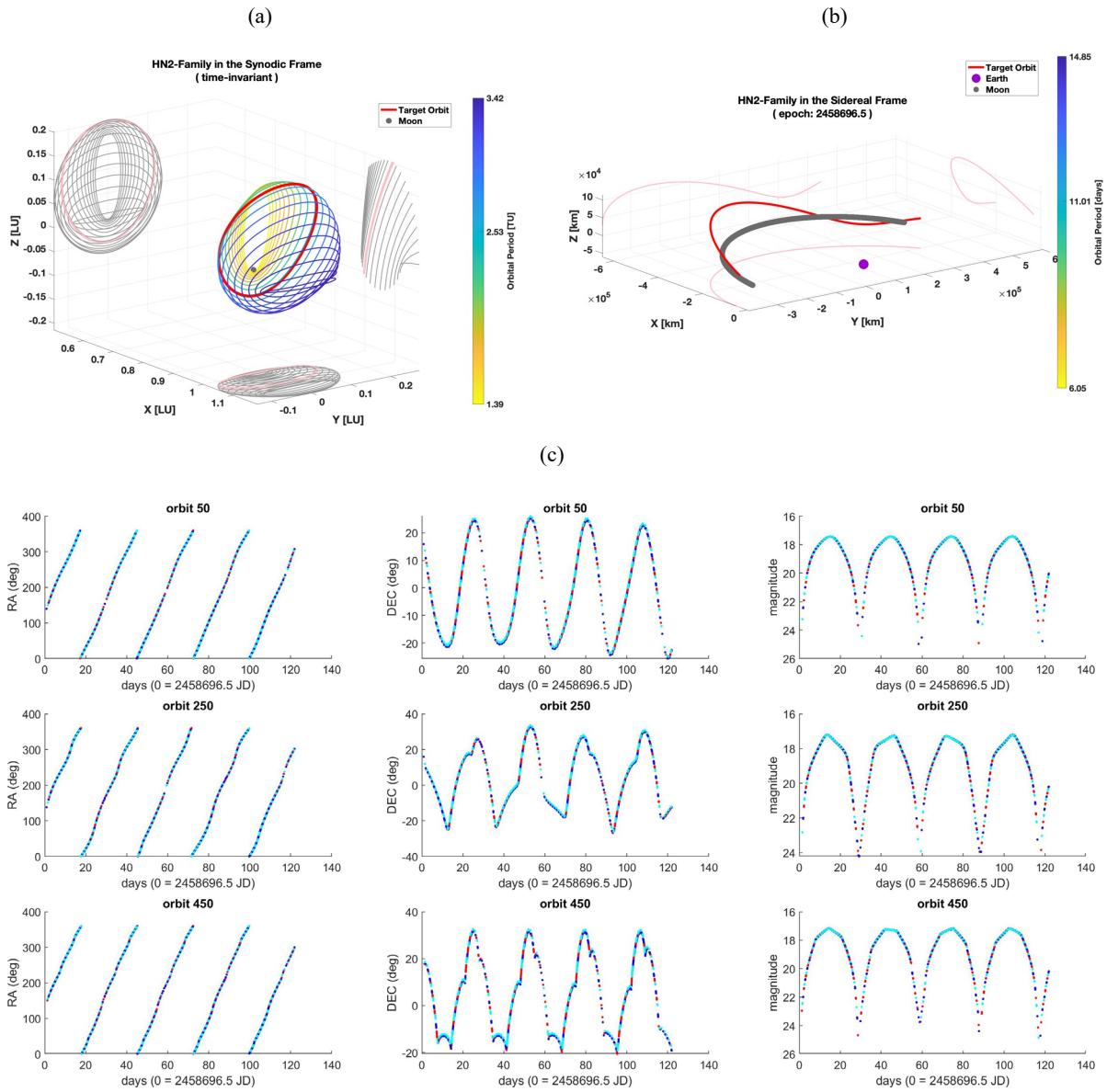


Figure 30. (a) HN2 family in the synodic frame and (b) sample HN2 target orbit in the sidereal frame for epoch 2019.08.01. (c) RA/DEC and magnitude observations over the entire 122 days for diffuse spheres in HN2 orbits 50, 250, and 450 (red: Maui, blue: Azores, cyan: Cocos Islands).

Table 18. HS2 family's ranges of notable parameters and list of connection points.

Period	Jacobi Constant	Connects to
6.05 – 14.85 days	3.02 – 3.15	Moon, L2

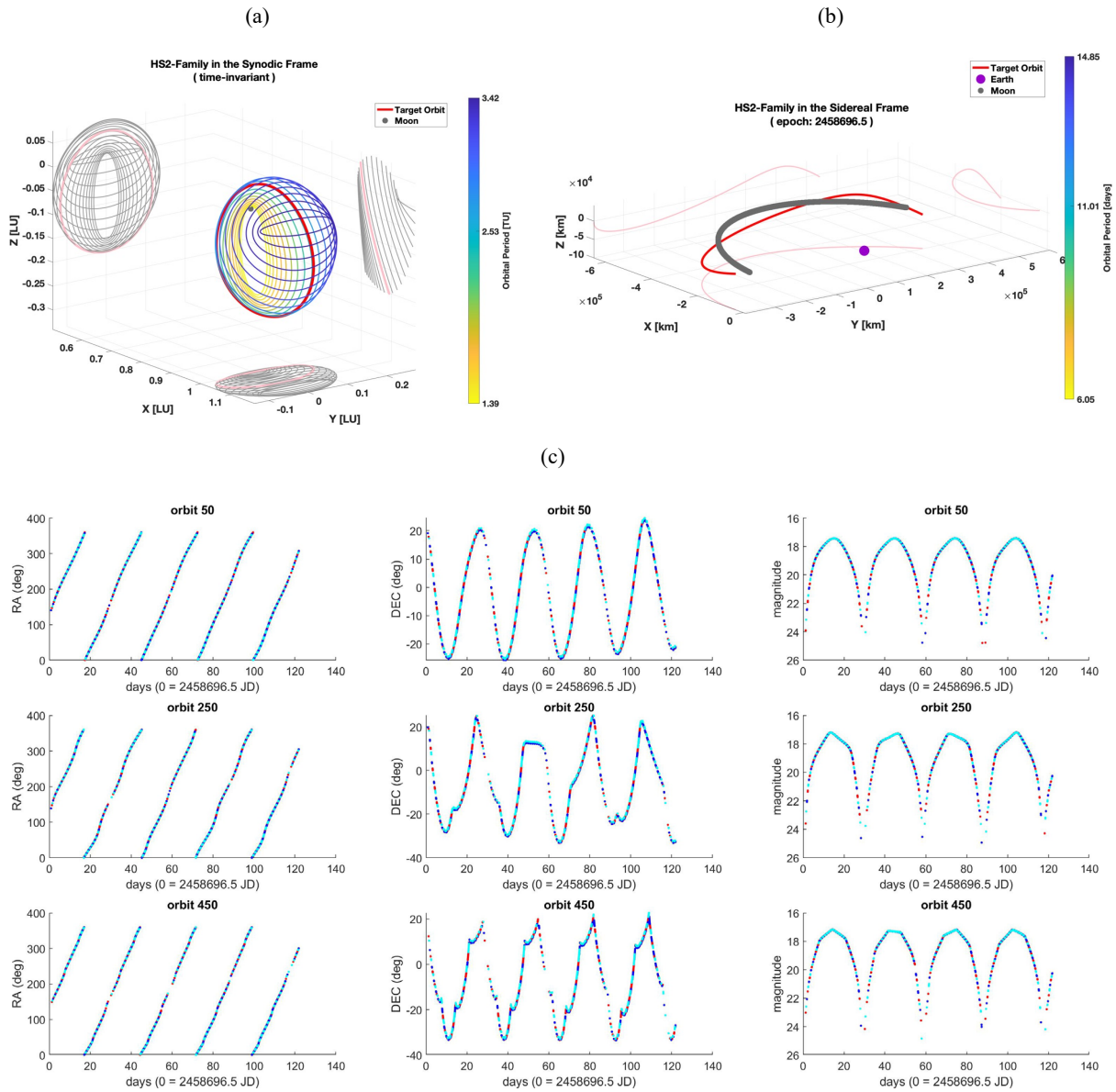


Figure 31. (a) HS2 family in the synodic frame and (b) sample HS2 target orbit in the sidereal frame for epoch 2019.08.01. (c) RA/DEC and magnitude observations over the entire 122 days for diffuse spheres in HS2 orbits 50, 250, and 450 (red: Maui, blue: Azores, cyan: Cocos Islands).

Table 19. HN3 family's ranges of notable parameters and list of connection points.

Period	Jacobi Constant	Connects to
20.19 – 27.13 days	1.05 – 2.42	Earth, L3

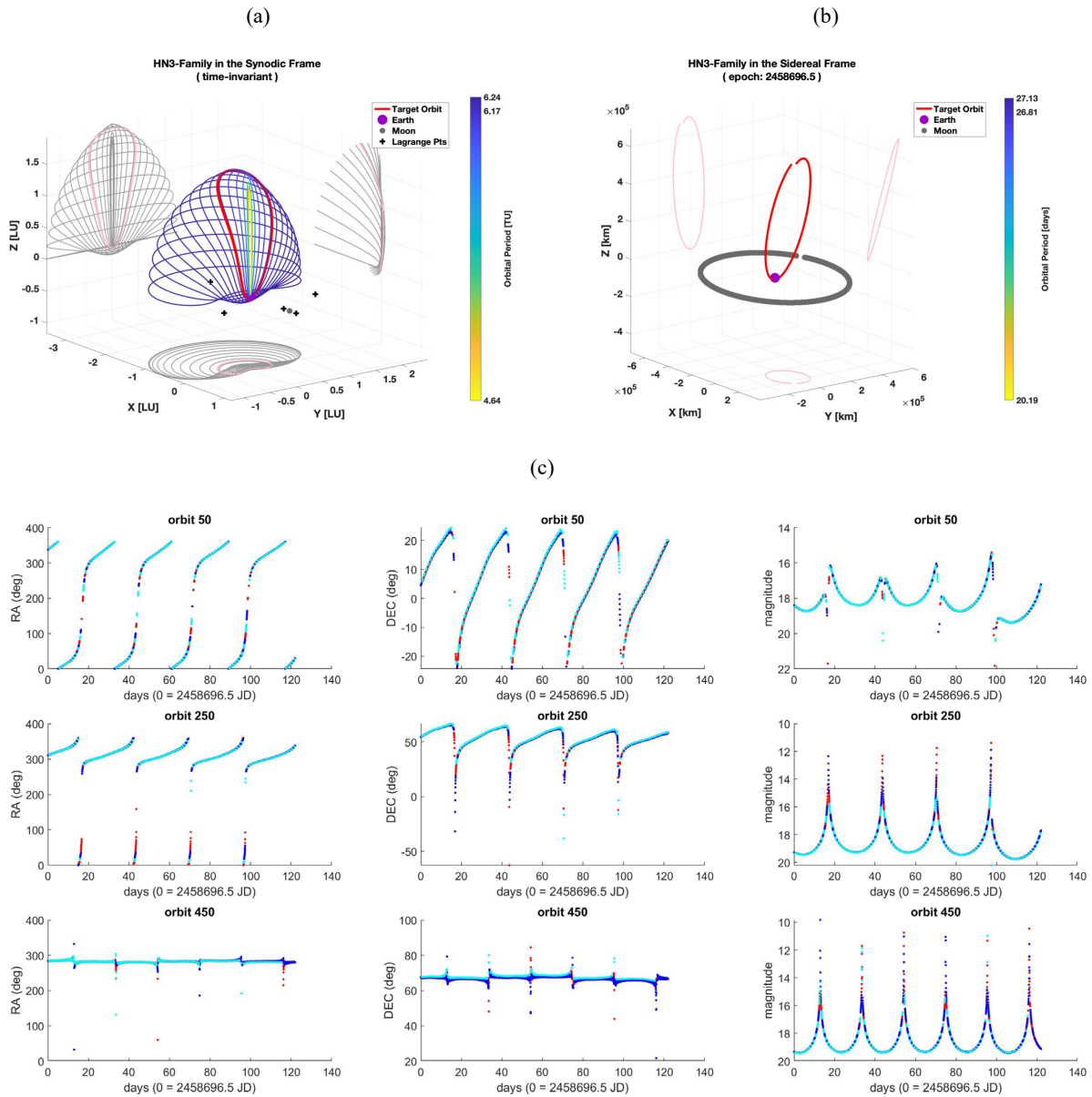


Figure 32. (a) HN3 family in the synodic frame and (b) sample HN3 target orbit in the sidereal frame for epoch 2019.08.01. (c) RA/DEC and magnitude observations over the entire 122 days for diffuse spheres in HN3 orbits 50, 250, and 450 (red: Maui, blue: Azores, cyan: Cocos Islands).

Table 20. HS3 family's ranges of notable parameters and list of connection points.

Period	Jacobi Constant	Connects to
20.19 – 27.13 days	1.05 – 2.42	Earth, L3

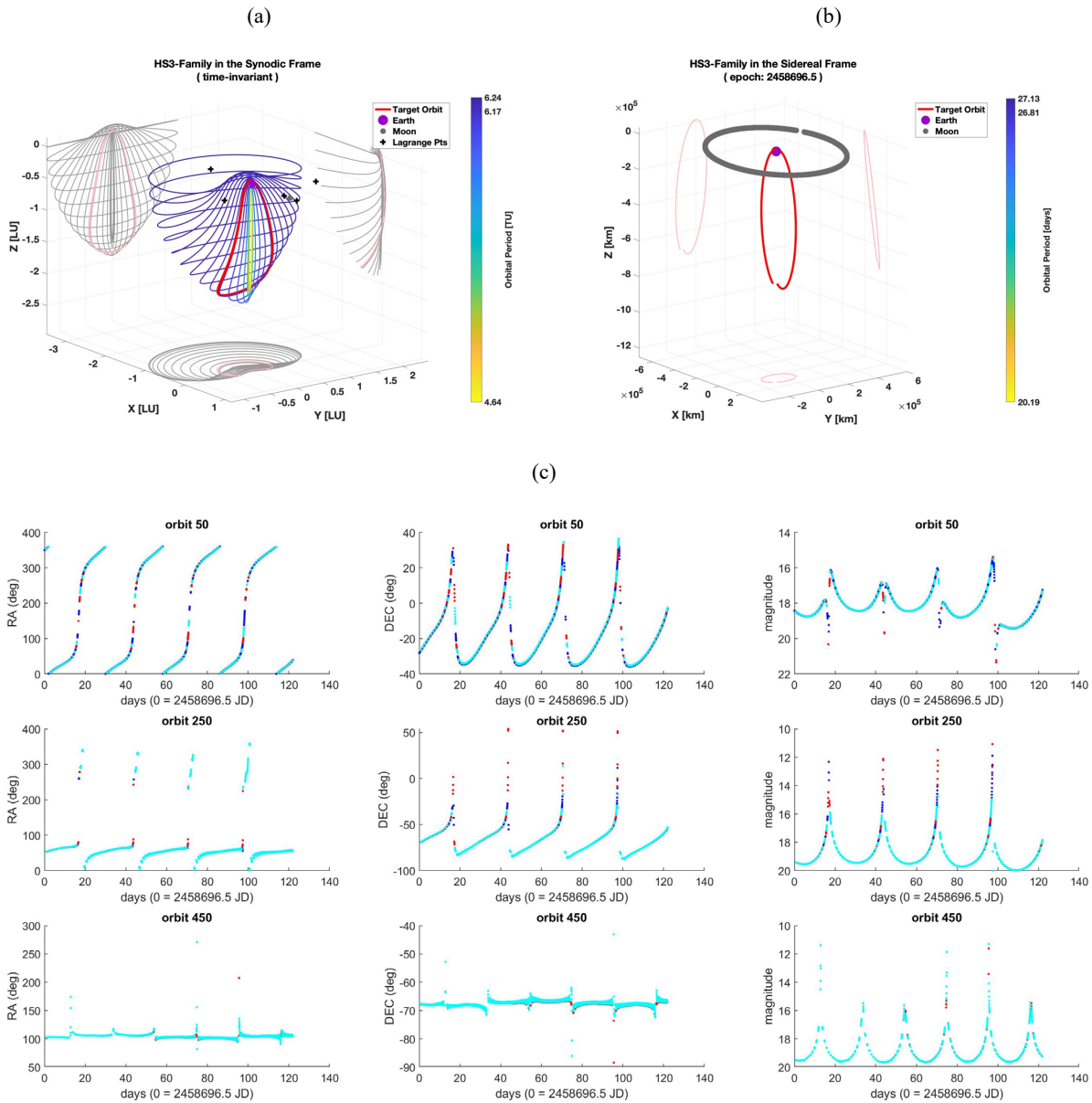


Figure 33. (a) HS3 family in the synodic frame and (b) sample HS3 target orbit in the sidereal frame for epoch 2019.08.01. (c) RA/DEC and magnitude observations over the entire 122 days for diffuse spheres in HS3 orbits 50, 250, and 450 (red: Maui, blue: Azores, cyan: Cocos Islands).

Table 21. L1 family's ranges of notable parameters and list of connection points.

Period	Jacobi Constant	Connects to
11.70 – 32.40 days	2.49 – 3.19	$\mathcal{L}1$, Moon, A1, H1

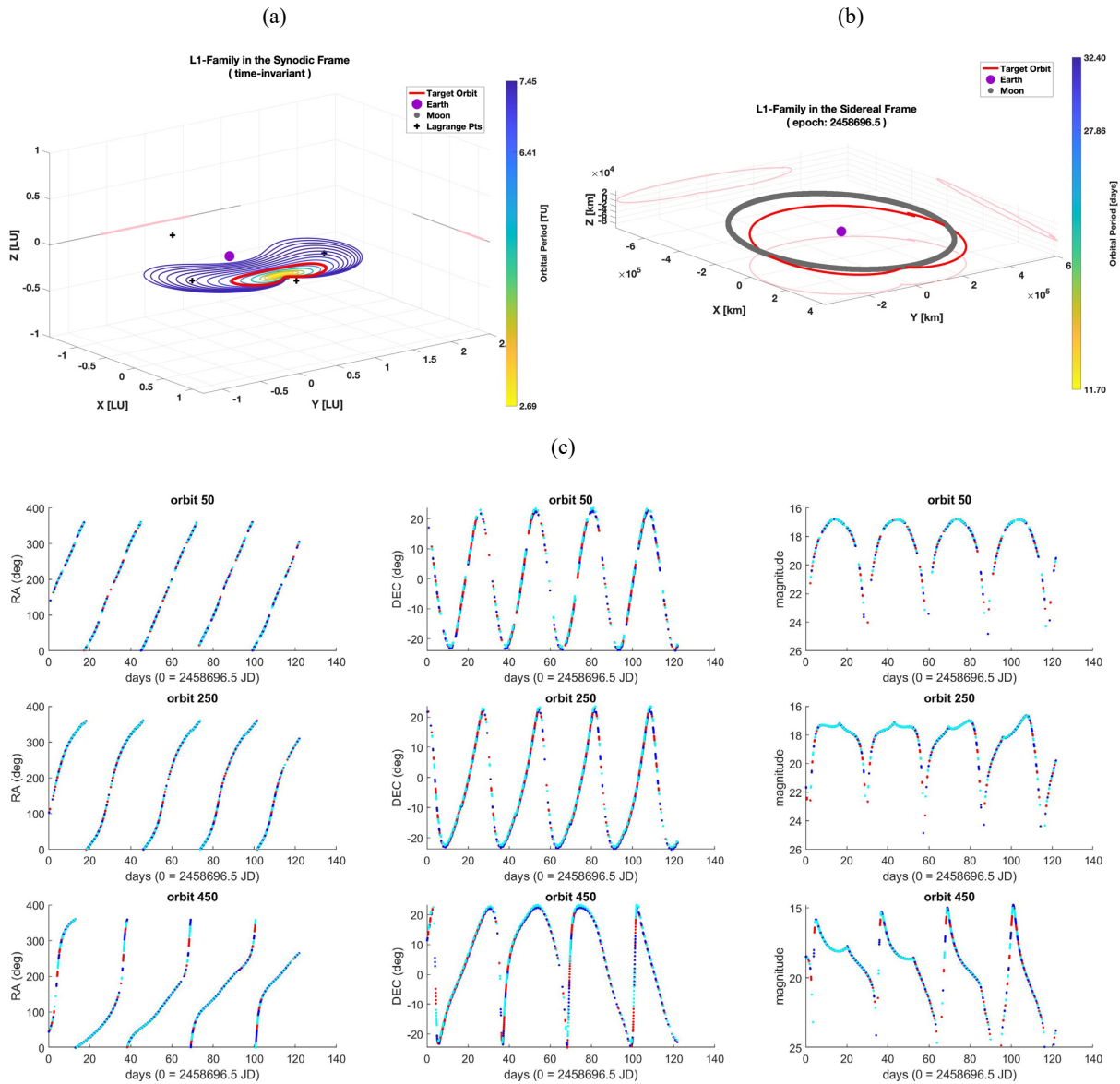


Figure 34. (a) L1 family in the synodic frame and (b) sample L1 target orbit in the sidereal frame for epoch 2019.08.01. (c) RA/DEC and magnitude observations over the entire 122 days for diffuse spheres in L1 orbits 50, 250, and 450 (red: Maui, blue: Azores, cyan: Cocos Islands).

Table 22. L2 family's ranges of notable parameters and list of connection points.

Period	Jacobi Constant	Connects to
14.67 – 40.39 days	2.78 – 3.17	$\mathcal{L}2$, Moon, A2, H2, R2

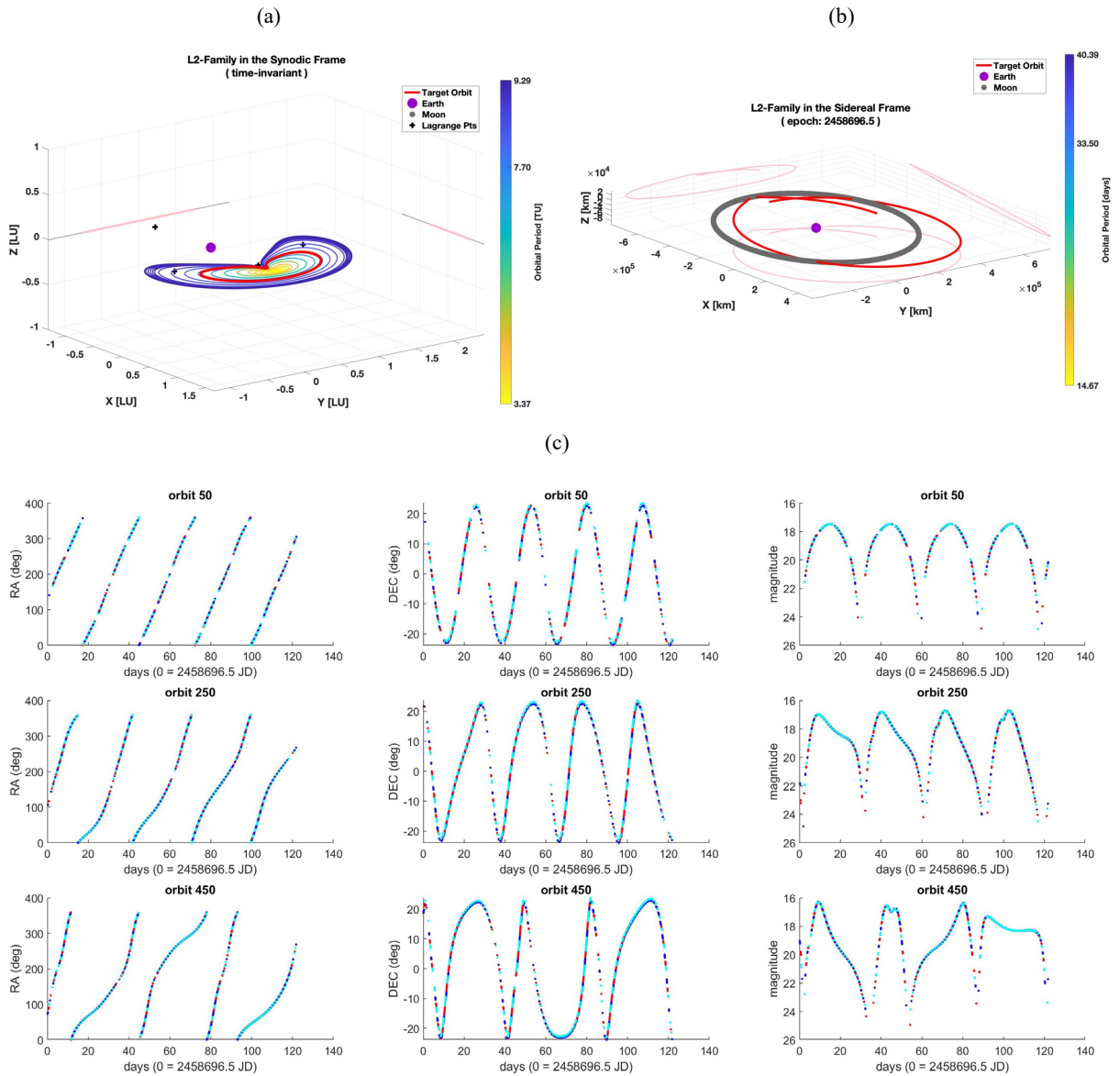


Figure 35. (a) L2 family in the synodic frame and (b) sample L2 target orbit in the sidereal frame for epoch 2019.08.01. (c) RA/DEC and magnitude observations over the entire 122 days for diffuse spheres in L2 orbits 50, 250, and 450 (red: Maui, blue: Azores, cyan: Cocos Islands).

Table 23. L3 family's ranges of notable parameters and list of connection points.

Period	Jacobi Constant	Connects to
27.04 – 27.26 days	1.68 – 3.01	$\mathcal{L}3$, Earth, A3, H3, S3

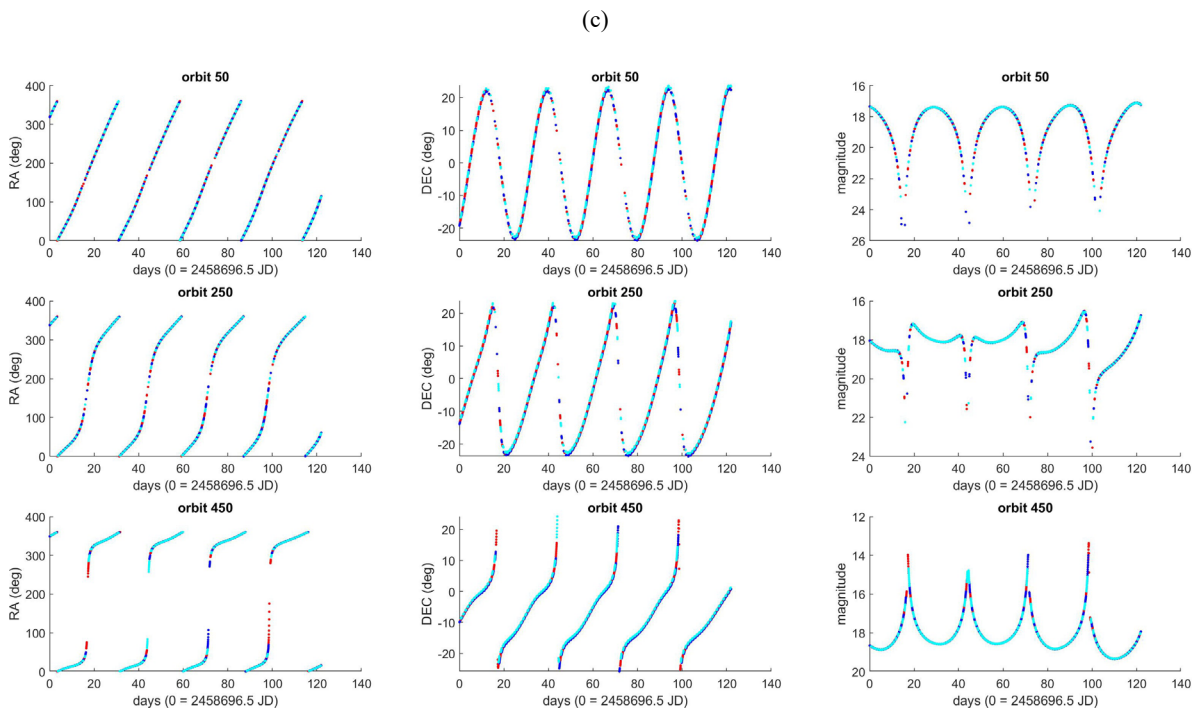
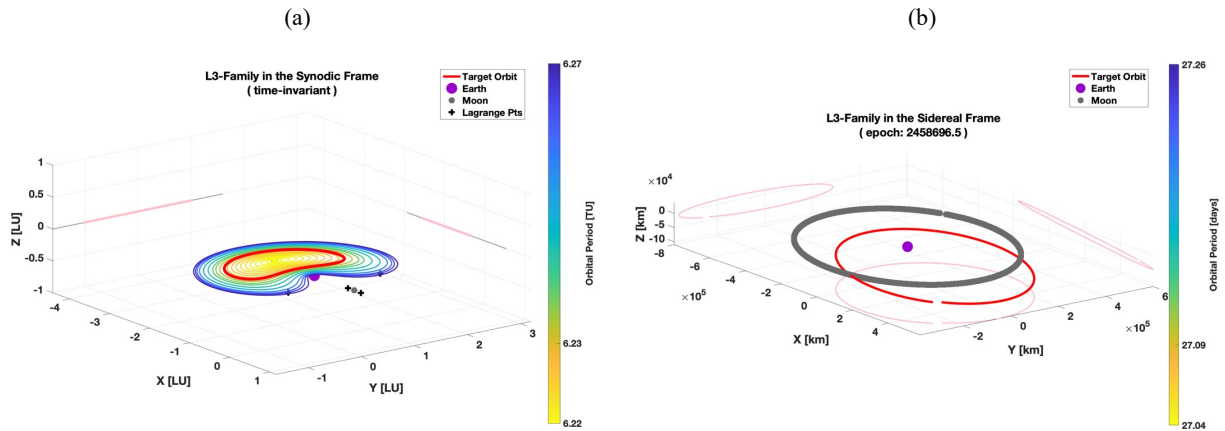


Figure 36. (a) L3 family in the synodic frame and (b) sample L3 target orbit in the sidereal frame for epoch 2019.08.01. (c) RA/DEC and magnitude observations over the entire 122 days for diffuse spheres in L3 orbits 50, 250, and 450 (red: Maui, blue: Azores, cyan: Cocos Islands).

Table 24. L4 family's ranges of notable parameters and list of connection points.

Period	Jacobi Constant	Connects to
91.62 – 114.03 days	2.29 – 3.00	$\mathcal{L}4, S3$

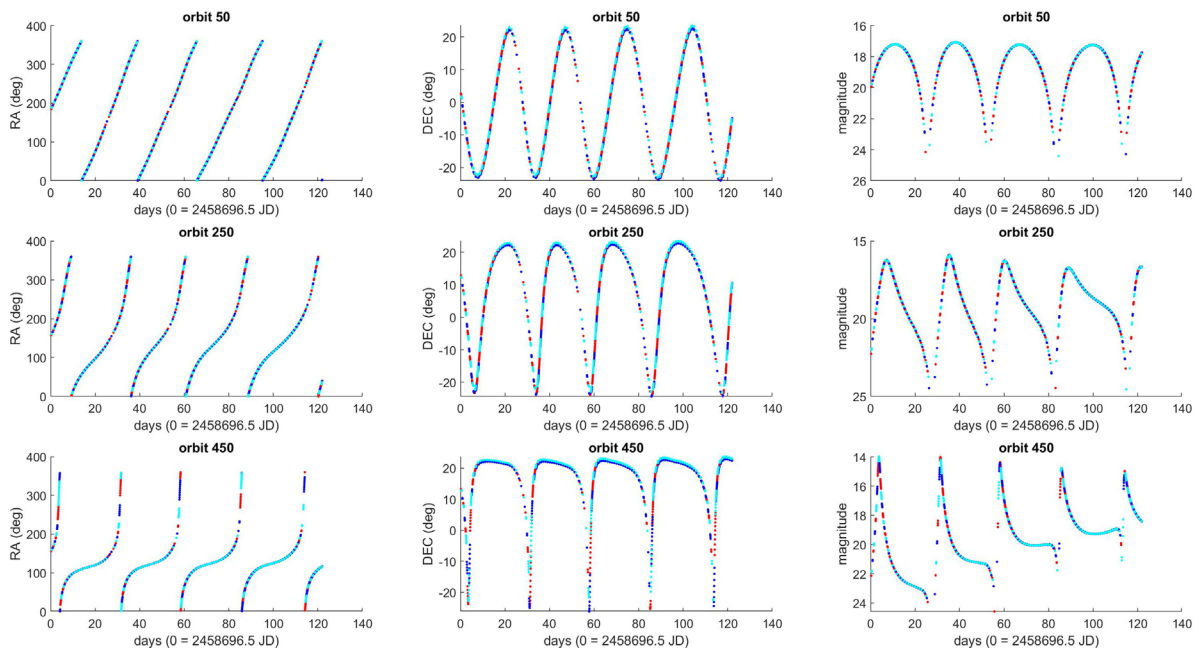
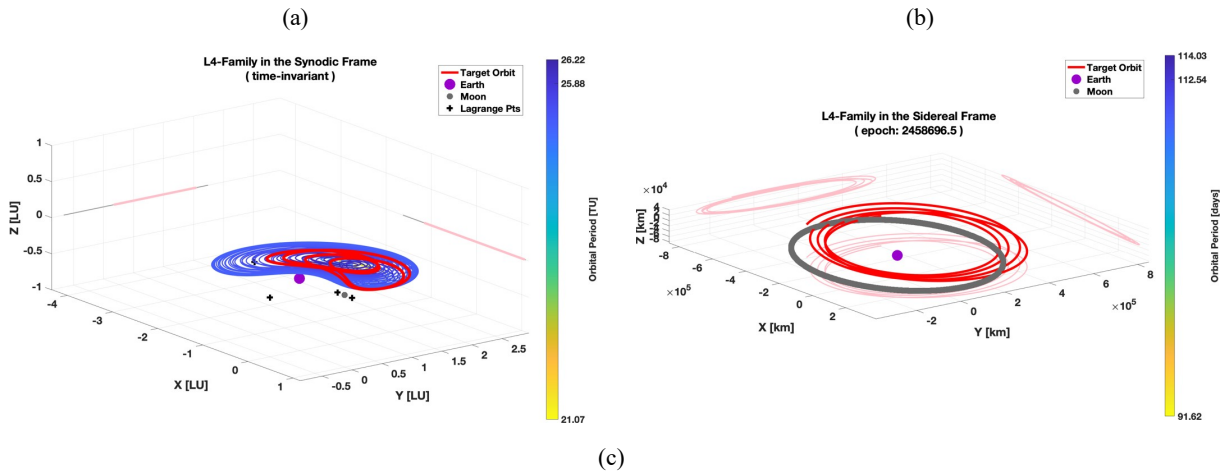


Figure 37. (a) L4 family in the synodic frame and (b) sample L4 target orbit in the sidereal frame for epoch 2019.08.01. (c) RA/DEC and magnitude observations over the entire 122 days for diffuse spheres in L4 orbits 50, 250, and 450 (red: Maui, blue: Azores, cyan: Cocos Islands).

Table 25. L5 family's ranges of notable parameters and list of connection points.

Period	Jacobi Constant	Connects to
91.62 – 114.03 days	2.29 – 3.00	$\mathcal{L}5, S3$

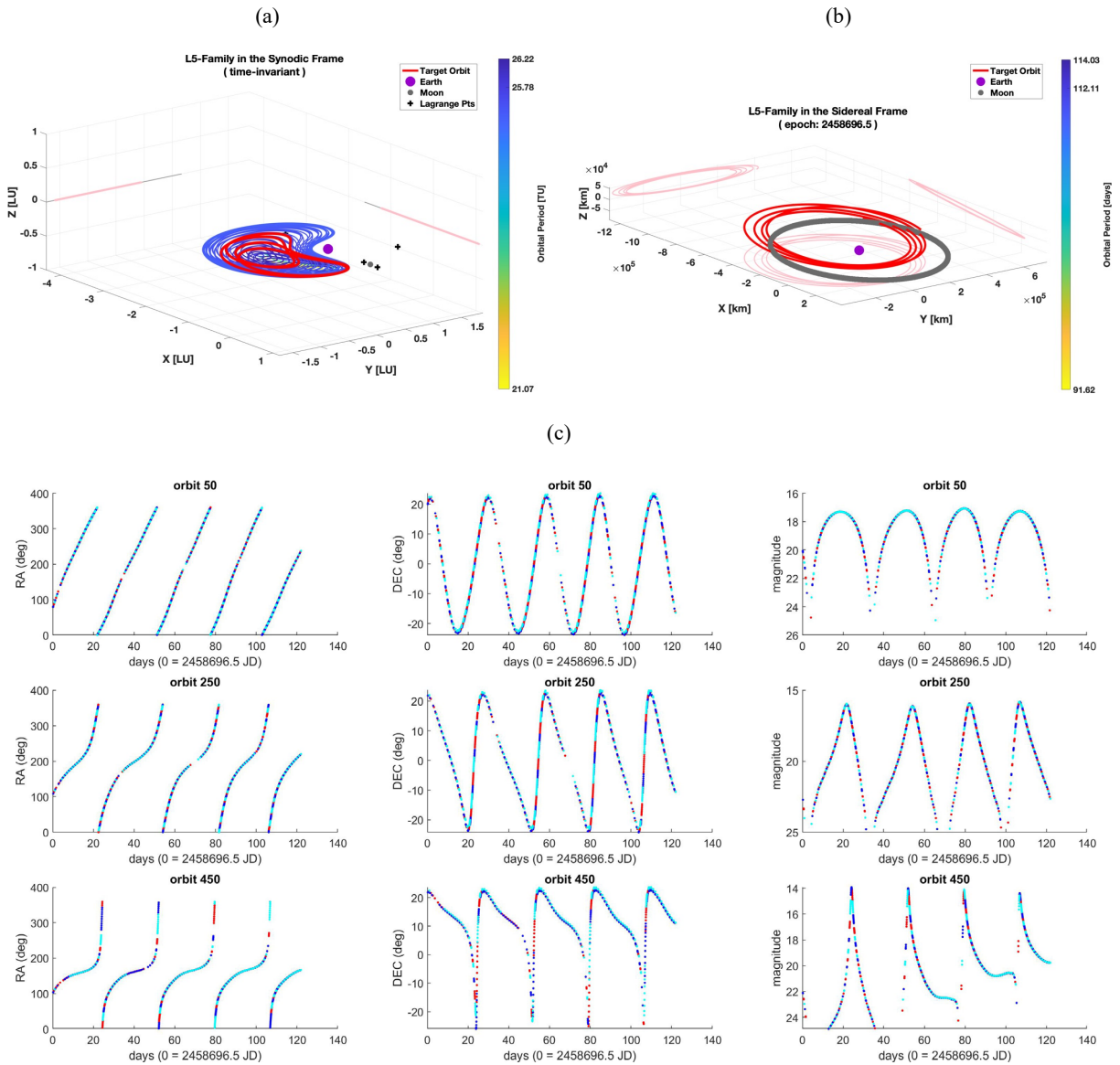


Figure 38. (a) L5 family in the synodic frame and (b) sample L5 target orbit in the sidereal frame for epoch 2019.08.01. (c) RA/DEC and magnitude observations over the entire 122 days for diffuse spheres in L5 orbits 50, 250, and 450 (red: Maui, blue: Azores, cyan: Cocos Islands).

Table 26. RN2 family's ranges of notable parameters and list of connection points.

Period	Jacobi Constant	Connects to
39.57 – 39.60 days	2.79 – 2.80	Moon, L2

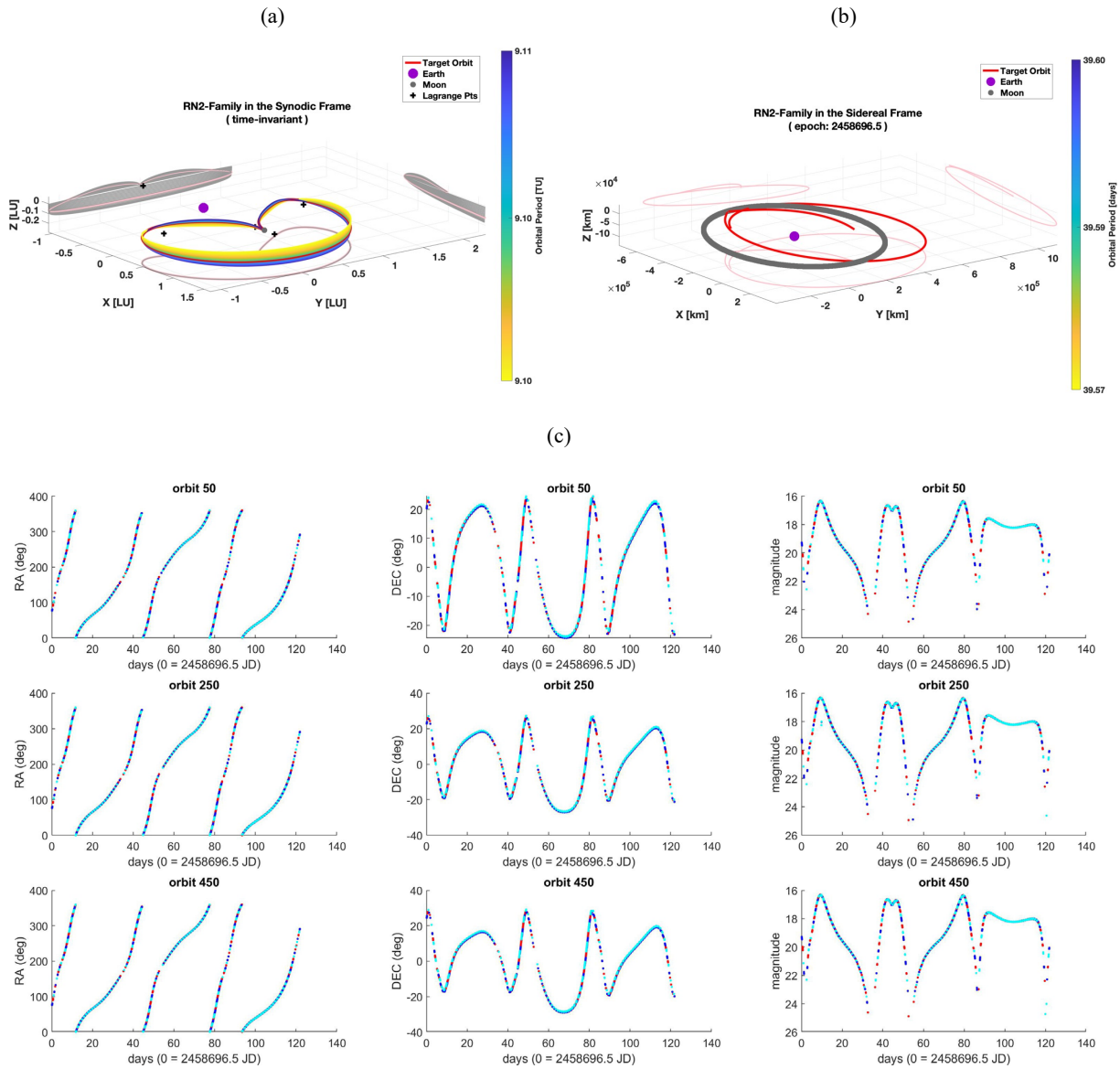


Figure 39. (a) RN2 family in the synodic frame and (b) sample RN2 target orbit in the sidereal frame for epoch 2019.08.01. (c) RA/DEC and magnitude observations over the entire 122 days for diffuse spheres in RN2 orbits 50, 250, and 450 (red: Maui, blue: Azores, cyan: Cocos Islands).

Table 27. RS2 family's ranges of notable parameters and list of connection points.

Period	Jacobi Constant	Connects to
39.57 – 39.60 days	2.79 – 2.80	Moon, L2

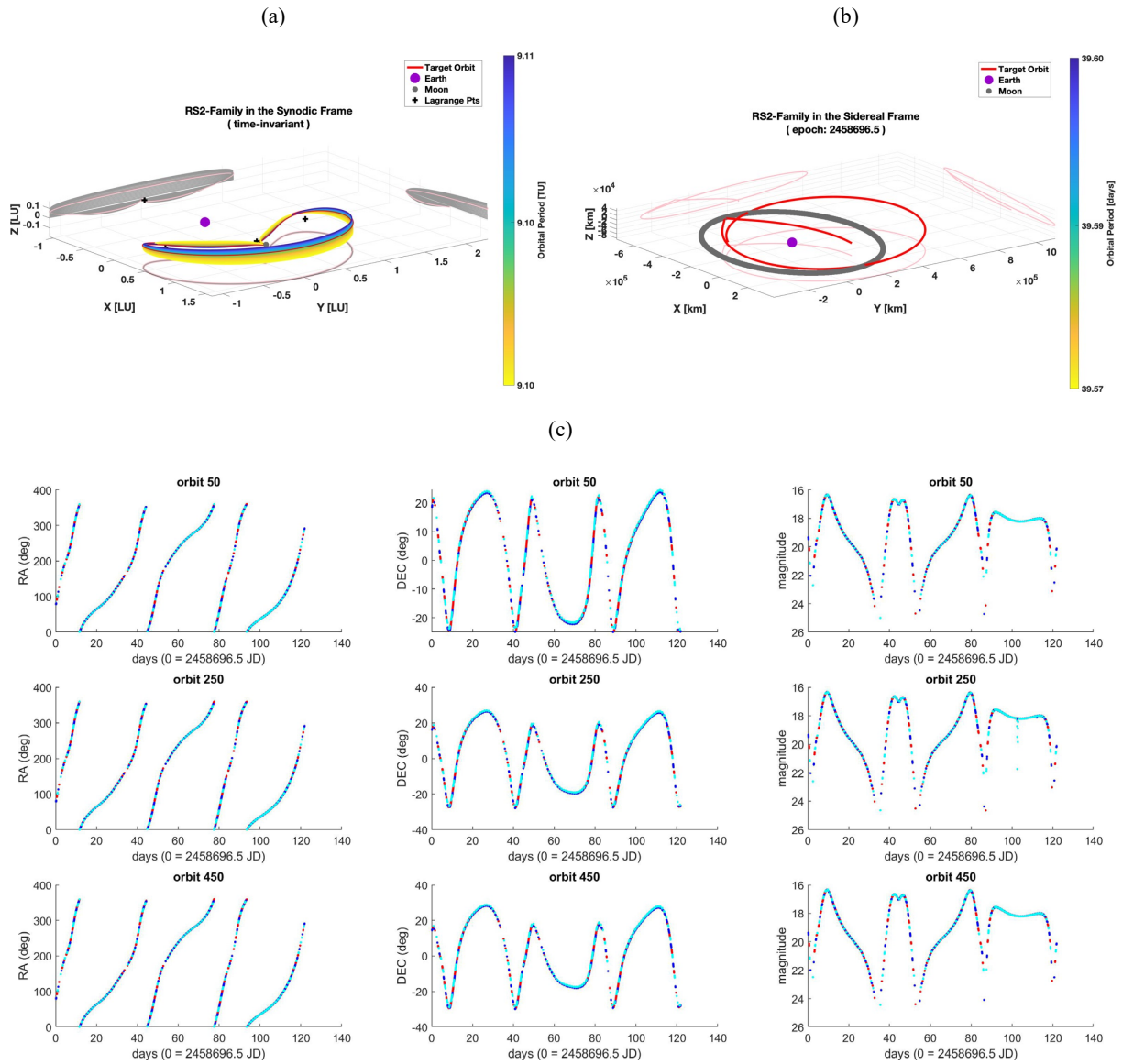


Figure 40. (a) RS2 family in the synodic frame and (b) sample RS2 target orbit in the sidereal frame for epoch 2019.08.01. (c) RA/DEC and magnitude observations over the entire 122 days for diffuse spheres in RS2 orbits 50, 250, and 450 (red: Maui, blue: Azores, cyan: Cocos Islands).

Table 28. S3 family's ranges of notable parameters and list of connection points.

Period	Jacobi Constant	Connects to
27.24 – 28.56 days	1.79 – 2.97	$\mathcal{L}4, \mathcal{L}5, L3, L4, L5$

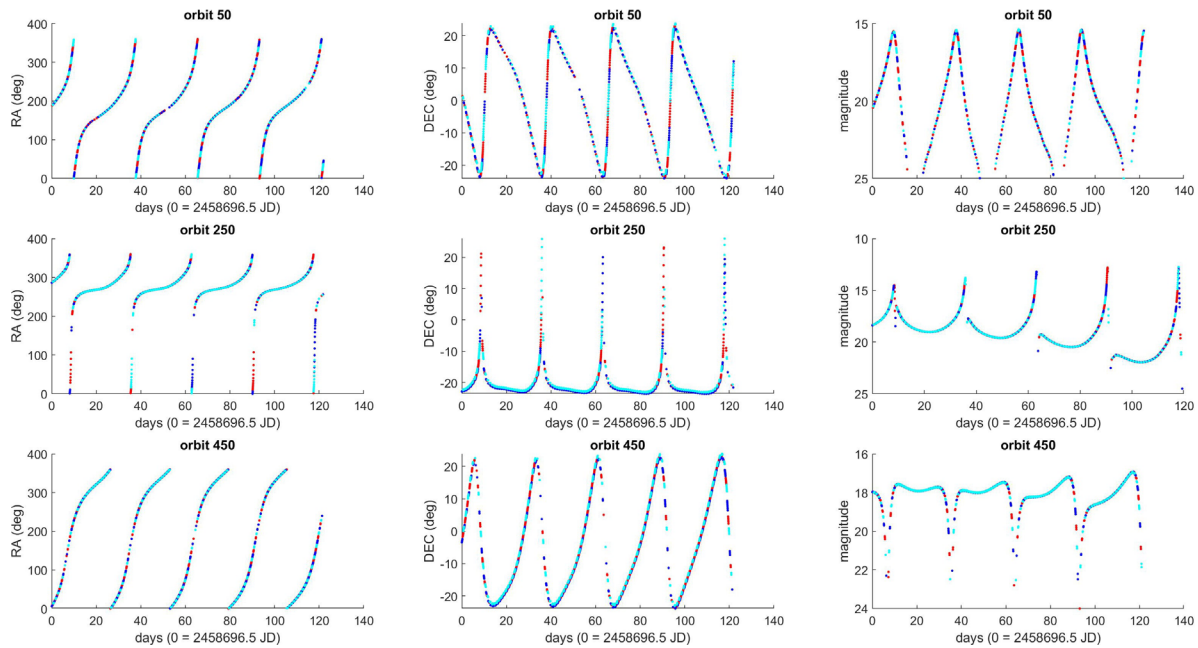
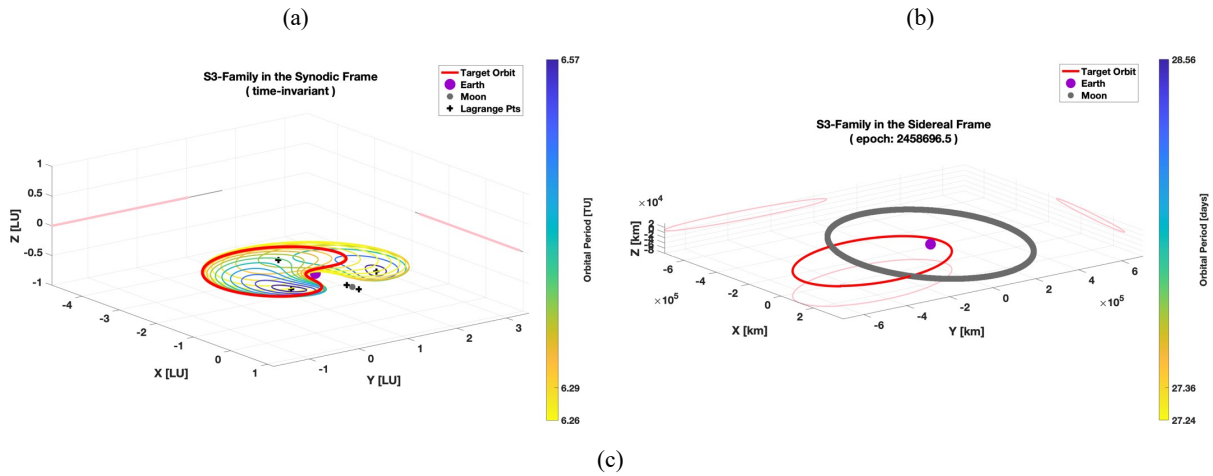


Figure 41. (a) S3 family in the synodic frame and (b) sample S3 target orbit in the sidereal frame for epoch 2019.08.01. (c) RA/DEC and magnitude observations over the entire 122 days for diffuse spheres in S3 orbits 50, 250, and 450 (red: Maui, blue: Azores, cyan: Cocos Islands).

Table 29. V1 family's ranges of notable parameters and list of connection points.

Period	Jacobi Constant	Connects to
12.04 – 27.39 days	(-0.84) – 3.19	$\mathcal{L}1, A1, B1, C1$

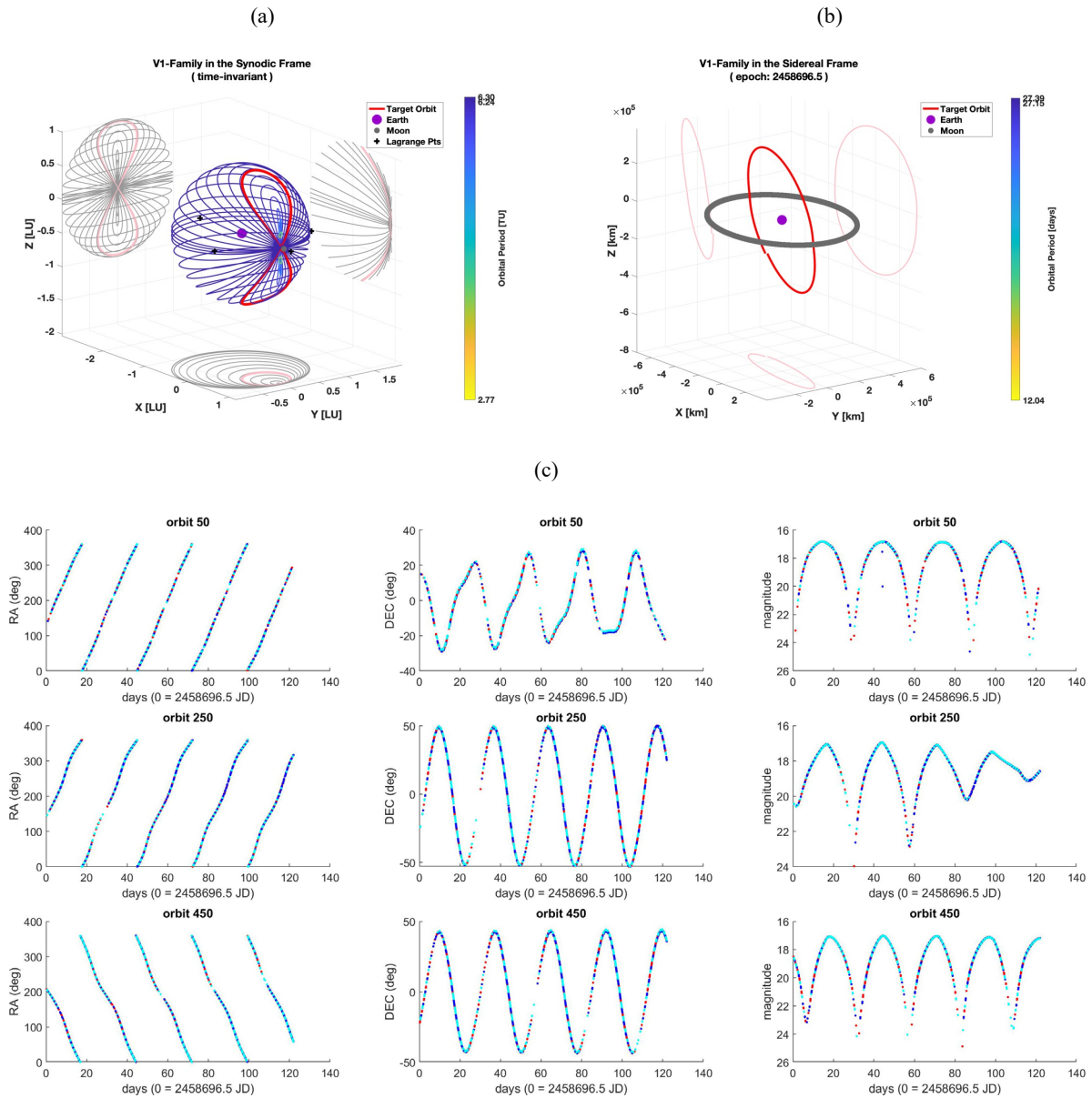


Figure 42. (a) V1 family in the synodic frame and (b) sample V1 target orbit in the sidereal frame for epoch 2019.08.01. (c) RA/DEC and magnitude observations over the entire 122 days for diffuse spheres in V1 orbits 50, 250, and 450 (red: Maui, blue: Azores, cyan: Cocos Islands).

Table 30. V2 family's ranges of notable parameters and list of connection points.

Period	Jacobi Constant	Connects to
15.30 – 27.38 days	(-1.13) – 3.17	$\mathcal{L}2$, A2, B2, C2

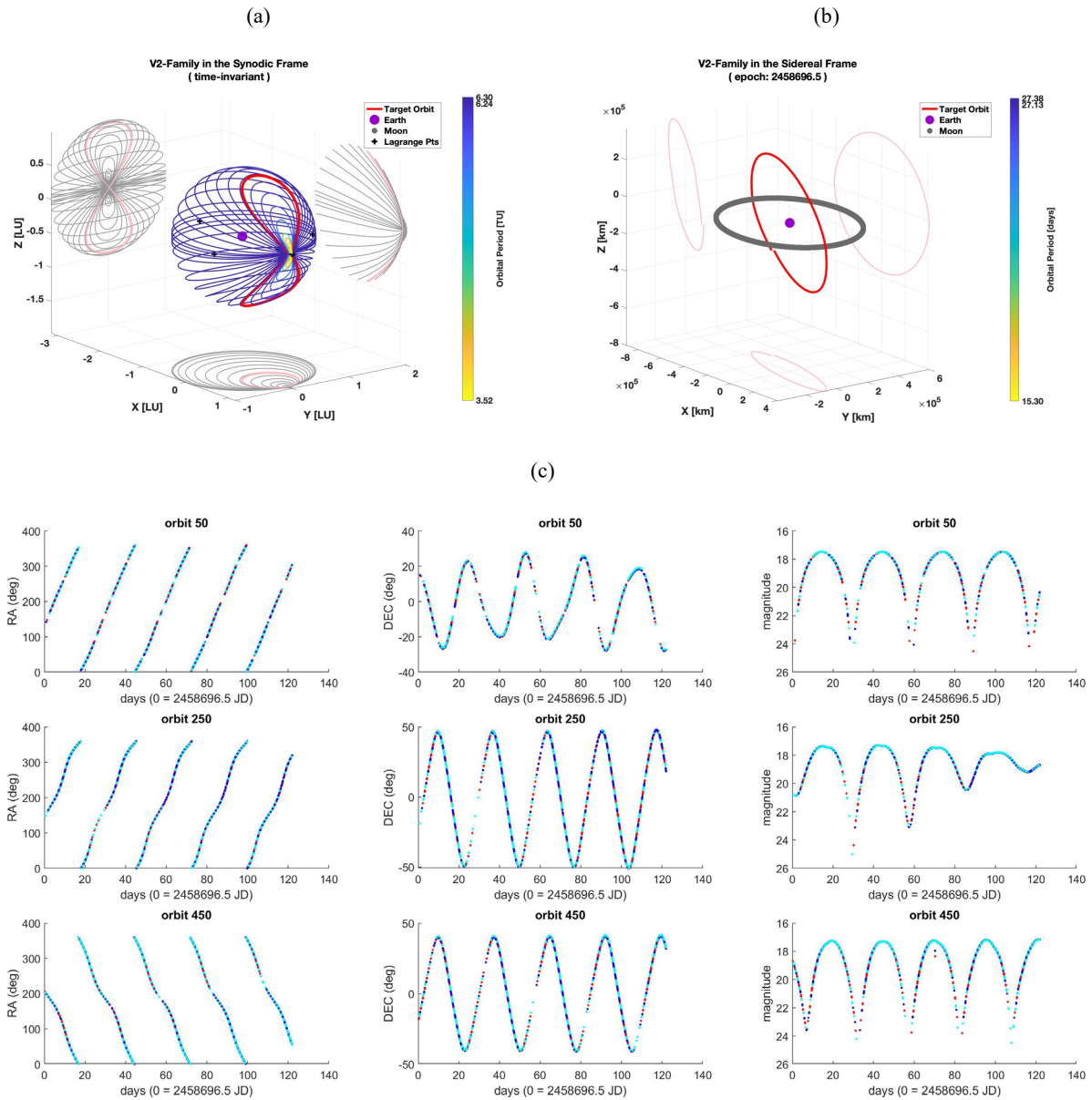


Figure 43. (a) V2 family in the synodic frame and (b) sample V2 target orbit in the sidereal frame for epoch 2019.08.01. (c) RA/DEC and magnitude observations over the entire 122 days for diffuse spheres in V2 orbits 50, 250, and 450 (red: Maui, blue: Azores, cyan: Cocos Islands).

Table 31. V3 family's ranges of notable parameters and list of connection points.

Period	Jacobi Constant	Connects to
27.18 – 30.32 days	(-1.33) – 3.01	$\mathcal{L}3$, A3, B3, C2, V4V5

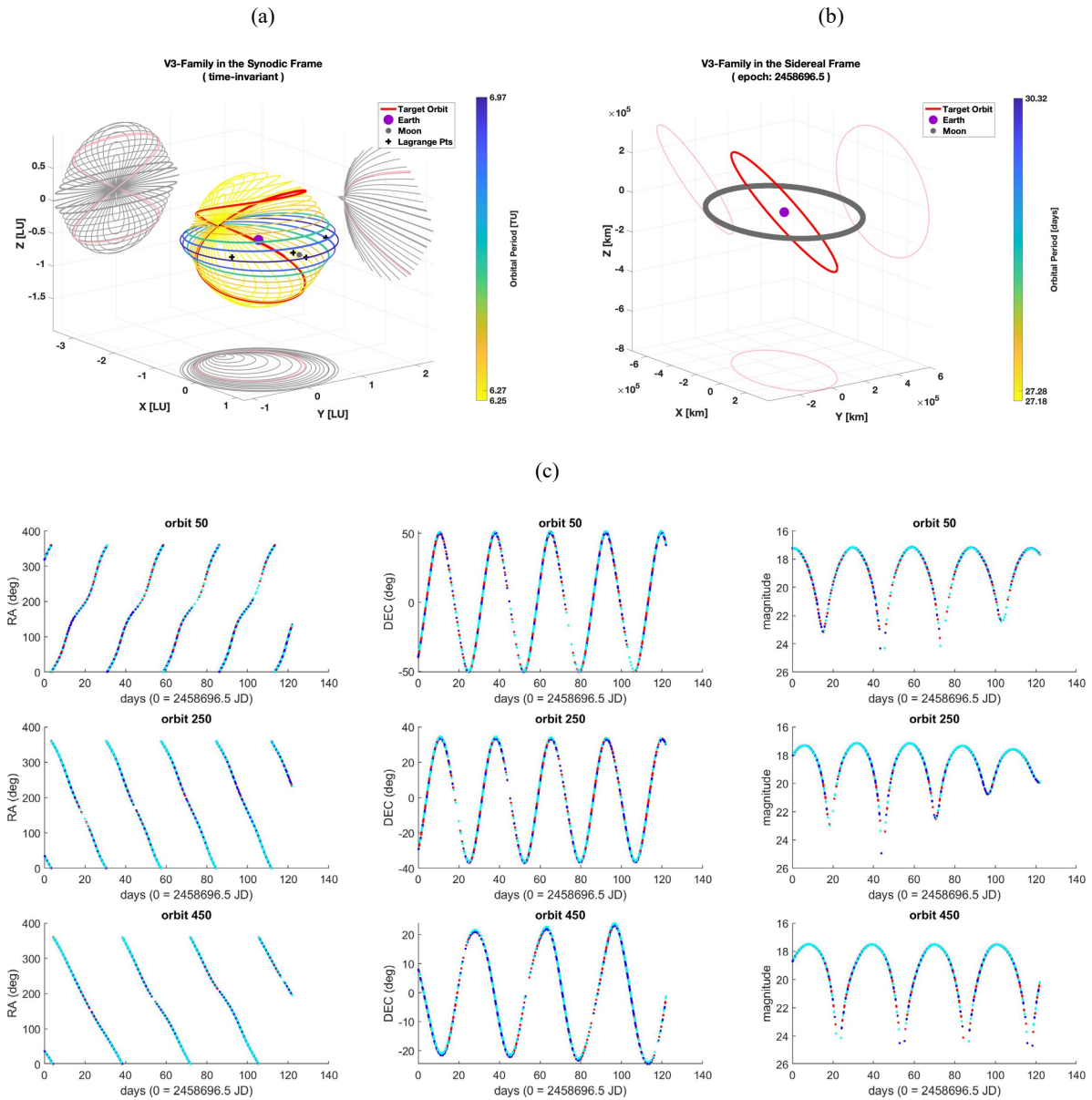


Figure 44. (a) V3 family in the synodic frame and (b) sample V3 target orbit in the sidereal frame for epoch 2019.08.01. (c) RA/DEC and magnitude observations over the entire 122 days for diffuse spheres in V3 orbits 50, 250, and 450 (red: Maui, blue: Azores, cyan: Cocos Islands).

Table 32. V4V5 family's ranges of notable parameters and list of connection points.

Period	Jacobi Constant	Connects to
27.32 – 27.44 days	(-0.64) – 2.99	$\mathcal{L}4, \mathcal{L}5, V3, W4W5$

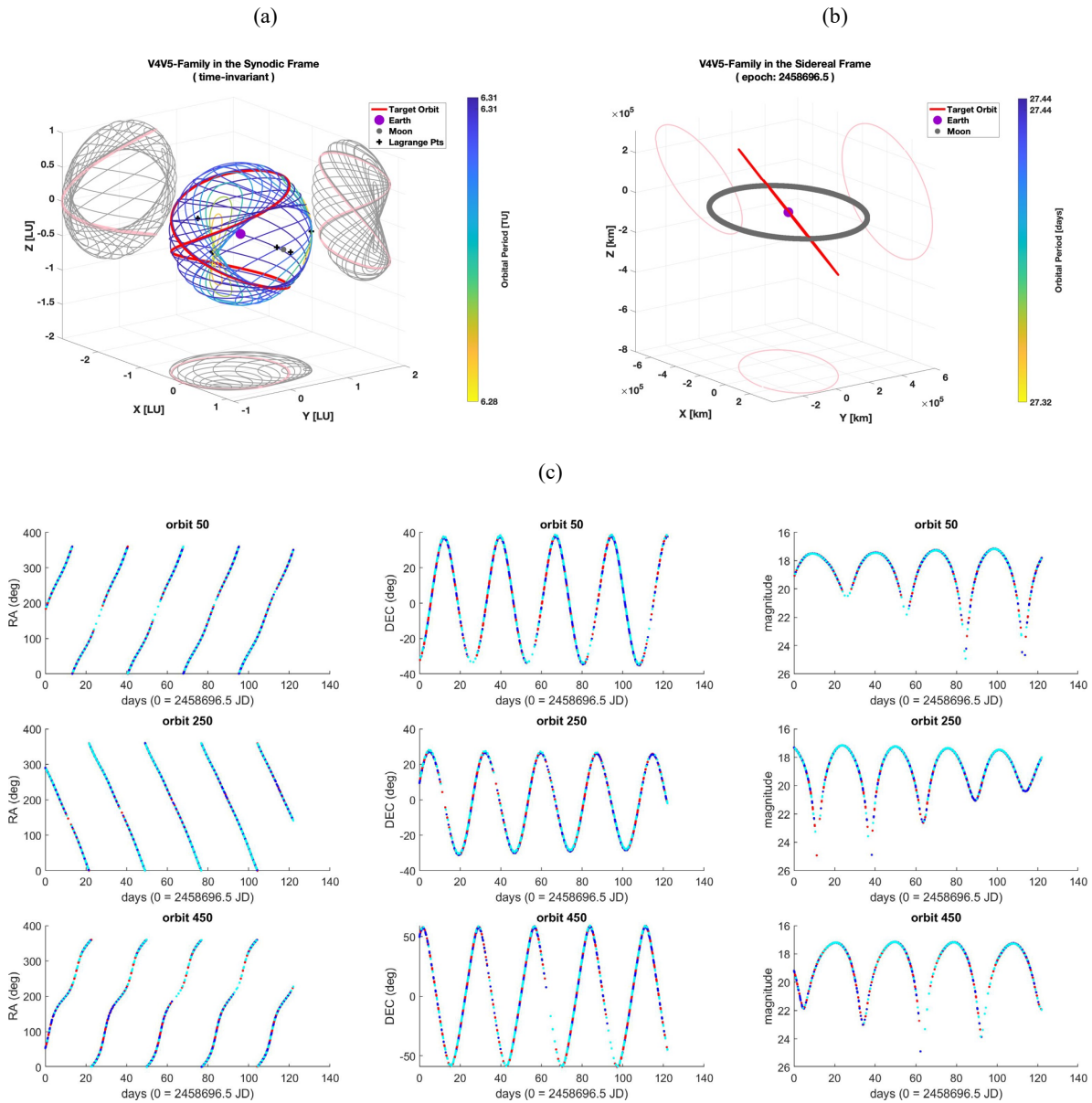


Figure 45. (a) V4V5 family in the synodic frame and (b) sample V4V5 target orbit in the sidereal frame for epoch 2019.08.01. (c) RA/DEC and magnitude observations over the entire 122 days for diffuse spheres in V4V5 orbits 50, 250, and 450 (red: Maui, blue: Azores, cyan: Cocos Islands).

Table 33. W4W5 family's ranges of notable parameters and list of connection points.

Period	Jacobi Constant	Connects to
9.26 – 27.38 days	1.94 – 2.95	H1, V4V5

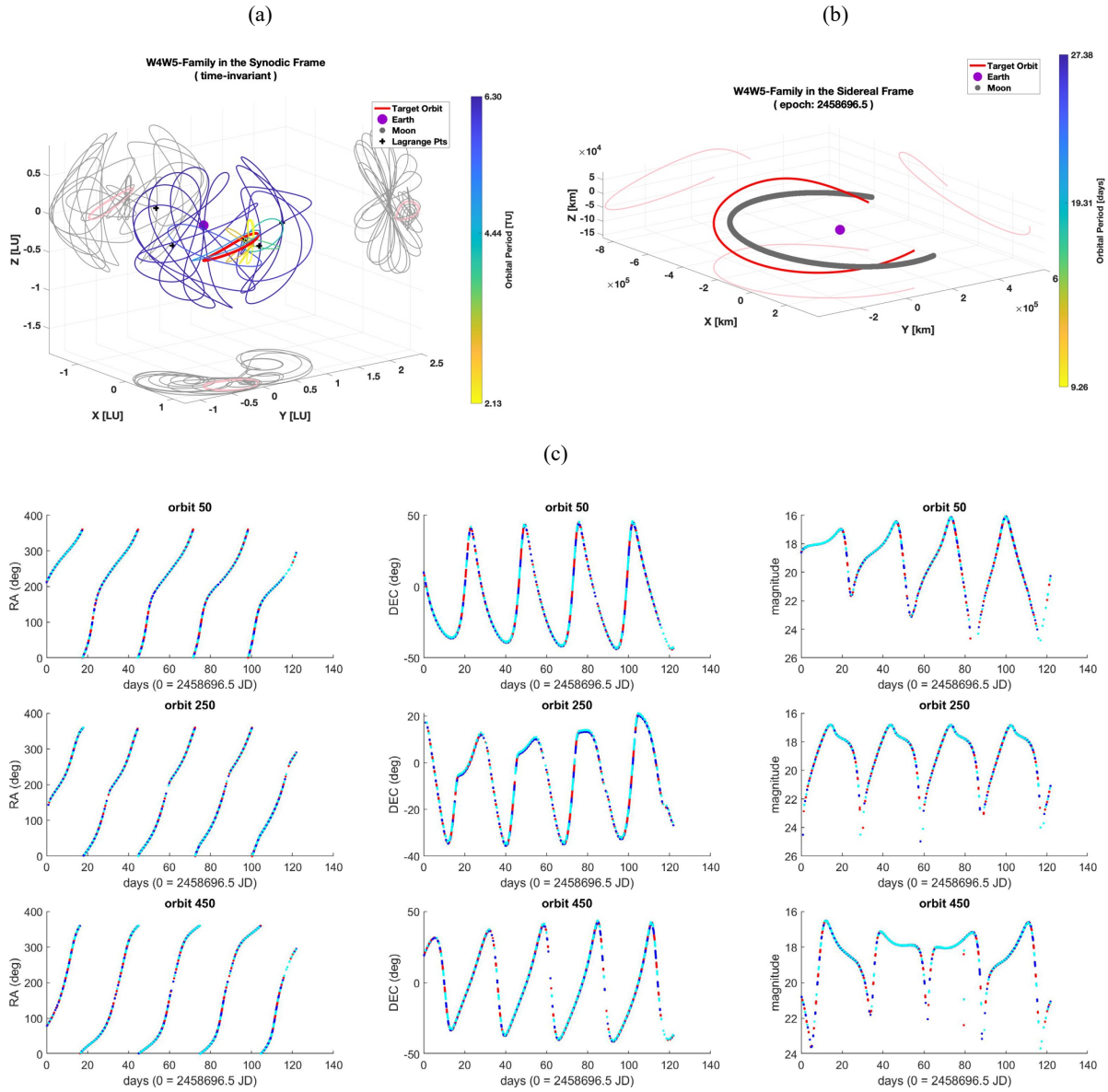


Figure 46. (a) W4W5 family in the synodic frame and (b) sample W4W5 target orbit in the sidereal frame for epoch 2019.08.01. (c) RA/DEC and magnitude observations over the entire 122 days for diffuse spheres in W4W5 orbits 50, 250, and 450 (red: Maui, blue: Azores, cyan: Cocos Islands).